Royal Netherlands Institute for Sea Research

This is a pre-copyedited, author-produced version of an article accepted for publication, following peer review.

Kusters, N., S. Groeskamp, and T. J. McDougall, 2024: Spiralling Inverse Method: A New Inverse Method to Estimate Ocean Mixing. *J. Phys. Oceanogr.*, 54, 2289–2309, https://doi.org/10.1175/JPO-D-24-0009.1.

Published version: https://doi.org/10.1175/JPO-D-24-0009.1

NIOZ Repository: http://imis.nioz.nl/imis.php?module=ref&refid=396538

[Article begins on next page]

The NIOZ Repository gives free access to the digital collection of the work of the Royal Netherlands Institute for Sea Research. This archive is managed according to the principles of the Open Access Movement, and the Open Archive Initiative. Each publication should be cited to its original source - please use the reference as presented.

Generated using the official AMS LaTeX template v6.1

Spiralling Inverse Method: A new inverse method to estimate ocean mixing

N. Kusters[a]

S. Groeskamp [a]

T.J. McDougall [b]

[a] *NIOZ Royal Netherlands Institute for Sea Research, Texel, The Netherlands*

[b] *School of Mathematics, University of New South Wales, Sydney, Australia*

Corresponding author: N. Kusters, niek.kusters@nioz.nl

ABSTRACT: Here we introduce the Spiralling Inverse Method (SIM) that provides estimates of the small-scale and mesoscale mixing strength. The SIM uses a vertical integral over a balance between the watermass transformation equation and the thermal wind equation. The result is an equation where all terms, except for the mixing strengths, can be obtained from hydrographic data of temperature and salinity. As an advantage, the SIM estimates the mixing strengths without the need of further knowledge of a reference velocity or streamfunction. Here we apply the SIM to a small region in the North Atlantic. We find that the estimates obtained by the SIM compare well to observations and other (inverse) estimates of the mixing strength. The SIM therefore has potential to improve and constrain parameterizations used for climate and ecosystem modelling using readily available hydrographic data.

SIGNIFICANCE STATEMENT: Ocean mixing is a combination of many different physical processes over a large range of scales in time (seconds to years) and space (millimeter to 100 km). Most of these processes are too small to compute in climate models and need to be simplified (parameterized). These parameterizations have a strong influence on climate projections and their shape and magnitude needs to be constrained using observations and indirect estimates of ocean mixing strength. The Spiralling Inverse Method (SIM) is a new method to obtain such constraints of mixing strengths using readily available observations of temperature and salinity. We here test the SIM and confirm its potential to improve mixing estimates and therewith ultimately climate simulations.

1. Introduction

Ocean mixing affects the uptake, transport and storage of tracers such as heat and carbon in the ocean, subsequently impacting the climate and its future changes (Clément et al. 2022; Melet et al. 2022; MacGilchrist et al. 2020; Tatebe et al. 2018; Pradal and Gnanadesikan 2014; Munk and Wunsch 1998). Ocean mixing is caused by many different physical processes that take place on a large range of spatiotemporal scales (Moum 2021; De Lavergne et al. 2022). This makes mixing difficult to observe, or resolve in numerical ocean models. Consequently, ocean models use parameterizations of mixing that determine its strength and distribution (Fox-Kemper et al. 2019). However, it turns out that models are very sensitive to unconstrained choices required for construction of these parameterizations (Pradal and Gnanadesikan 2014; Holmes et al. 2022). These mixing parameterizations can be improved by using observationally based constraints (Fox-Kemper et al. 2019).

In studies of ocean mixing, and especially in numerical modelling, mixing parameterizations generally split mixing into mesoscale isoneutral mixing of which the strength is represented by a diffusion coefficient K, and small-scale dianeutral mixing of which the strength is given by the diffusion coefficient D (Fox-Kemper et al. 2019; Griffies 1998). Isoneutral (dianeutral) movement refers to movement along (across) surfaces of constant neutral density rather than along (across) surfaces of potential density, which is referred to by isopycnal (diapycnal) movement. For a more complete description of the differences between isoneutral (dianeutral) and isopycnal (diapycnal) the reader is referred to McDougall (1987a). The mesoscale mixing is directed along neutral tangent planes, while small-scale mixing is isotropic, and often approximated as vertical or dianeutral (McDougall et al. 2014). Neutral surfaces are surfaces along which a water parcel can be moved a small distance without experiencing a buoyant restoring force (McDougall 1987a). The mesoscale isoneutral diffusion coefficient K acts on scales of $O(10-100km)$ and is characterised by typical values ranging between $O(10^1-10^3\ m^2\ s^{-1})$, though higher values of $O(10^4\ m^2\ s^{-1})$ can occur (Abernathey et al. 2021). The dianeutral diffusion coefficient D has many different sources, such as wind-generated mixing by the breaking of near-inertial waves (Alford et al. 2016), the dissipation of internal tides (De Lavergne et al. 2019) or the dissipation of lee-waves (MacKinnon 2013; Legg 2021). Typical values of D are in the order of $O(10^{-6}-10^{-3}\ m^2\ s^{-1})$ (Waterhouse et al. 2014), with the lowest values being found in the quiescent ocean interior, and increased values over rough topography. Though values of D can in some cases even exceed $10^{-3}\ m^2\ s^{-1}$. Here we aim to find observationally based constraints for the parameterizations of the diffusion coefficients with the help of a new inverse method.

Inverse methods traditionally have been developed and used to obtain estimates of large scale circulation and transport rates from hydrographic data, e.g. the box inverse method (Wunsch 1978), the beta-spiral inverse method (Stommel and Schott 1977; Schott and Stommel 1978) and the Bernouilli inverse method (Killworth 1986). At a later stage the existing methods were extended by including the dianeutral diffusion coefficient D (Ganachaud and Wunsch 2000; Sloyan and Rintoul 2000, 2001) or both K and D (Zhang and Hogg 1992; Hautala 2018). Yet, even for these methods, the main focus remained on solving the circulation, leading to less accurate mixing results (Zika et al. 2010a). More recently developed inverse methods were specifically designed to estimate mixing coefficients (Zika et al. 2010a; Groeskamp et al. 2014, 2017; Mackay et al. 2018). Regardless of these improvements, these inverse methods also required the estimation of streamfunctions or velocities, which can potentially add more uncertainty and error to the mixing estimates. In this study, we will provide the derivation of the new Spiralling Inverse Method (SIM) that is explicitly designed to estimate only the diffusion coefficients K and D, without the need to estimate any other variables.

The Spiralling Inverse Method (SIM) is a vertical integral over a balance on a neutral tangent plane, between the water mass transformation equation and the thermal wind balance. The SIM uses the spiralling of temperature contours on neutral surfaces, with depth, to eliminate an unknown reference velocity. The result is a balance where all terms can be determined based on hydrographic data except for the diffusion coefficients that we estimate using the inverse method. The SIM also differs from other inverse methods, as it is a semi-local method. That is, one needs only the isoneutral gradients of T, S, p on a vertical cast. In contrast, other existing methods are either global (Groeskamp et al. 2014, 2017), basin-scale (Mackay et al. 2018) or regional (Zika et al. 2010b; Hautala 2018).

This paper is structured as follows; in Section 2 we will introduce the new inverse method. Section 3 is reserved for a description of the data that is used in an application of this method. Section 4 focusses on the inversion process of the method, while the results of applying the method to a region in the North Atlantic are presented in Section 5. Section 6 then compares these results to other studies in this area. Discussions and conclusions follow in Section 7.

2. Methods - The Spiralling Inverse Method

The Spiralling Inverse Method (SIM) is an inverse method that produces estimates for the isoneutral diffusion coefficient K and the dianeutral diffusion coefficient D. These estimates are obtained using observed temperature and salinity data. Here we will use Conservative Temperature, Θ ([°C]), and Absolute Salinity, S_A ([g kg^{-1}]), as variables for 'heat' and salinity respectively. Conservative Temperature is proportional to potential enthalphy (by the constant heat capacity factor c_p^0, in [J kg^{-1} K^{-1}]), representing the heat content per unit mass of seawater (McDougall 2003; Graham and McDougall 2013). Absolute Salinity is designed to approximate the ratio between the mass of dissolved material and the mass of seawater ([g kg^{-1}], (Wright et al. 2011; McDougall et al. 2012)). It is measured on the Reference Composition Salinity Scale (Millero et al. 2008). It is also the salinity variable of IOC et al. (2010), the thermodynamic description of seawater. These variables are considered on neutral tangent planes. Because the neutrality condition defines Θ and S_A contours to be aligned, the direction in the neutral tangent plane normal to these contours (or cross-contour direction) is defined as:

$$\boldsymbol{\tau} = \frac{\nabla_n \Theta}{|\nabla_n \Theta|} \equiv \frac{\nabla_n S_A}{|\nabla_n S_A|}. \quad (1)$$

Here ∇_n is the two-dimensional non-orthogonal projected operator in the neutral tangent plane. Note that this vector has only horizontal components, as described by McDougall (1987a) and McDougall et al. (2014).

Ocean mixing is dominated by downgradient diffusive fluxes (Redi 1982; McDougall 1987a), therefore it makes sense to write the Eulerian-averaged horizontal velocity vector $\overline{\mathbf{v}}$, in terms of its cross-contour and along-contour components (indicated by superscript $\perp$ and $||$, respectively) in the neutral tangent plane (McDougall 1995):

$$\overline{\mathbf{v}} = v^{\perp}\boldsymbol{\tau} + v^{||}\mathbf{k}\times\boldsymbol{\tau}, \tag{2}$$

with $\mathbf{k} = (0,0,1)$ being the vertical unit vector, and where

$$v^{\perp} = \overline{\mathbf{v}}\cdot\tau, \quad \text{and} \quad v^{||} = \overline{\mathbf{v}}\cdot(\mathbf{k}\times\boldsymbol{\tau}) \tag{3}$$

Taking the vertical derivative of $v^{\perp}$ gives

$$v_z^{\perp} = \overline{\mathbf{v}}_{\mathbf{z}}\cdot\boldsymbol{\tau} + \overline{\mathbf{v}}\cdot\boldsymbol{\tau}_{\boldsymbol{z}}. \tag{4}$$

a. Finding an expression for $v_z^{\perp}$ using the thermal wind balance.

$\overline{\mathbf{v}}_{\mathbf{z}}$, and with that also $v_z^{\perp}$ can be found using the thermal wind balance. The thermal wind equation can be found by taking the vertical derivative of the geostrophic velocity and combining it with the hydrostatic balance. This can be expressed as (see also Section 3.12.3 of IOC et al. (2010)):

$$\overline{\mathbf{v}}_{\mathbf{z}} = -\frac{g}{f\,\rho}\mathbf{k}\times\nabla_p\rho. \tag{5}$$

Here, f is the Coriolis parameter, g the gravitational acceleration and ρ is density. Vertically integrating $\overline{\mathbf{v}}_{\mathbf{z}}$ gives another expression for $\overline{\mathbf{v}}$:

$$\overline{\mathbf{v}} = \underbrace{\int_{z_l}^{z_u}\overline{\mathbf{v}}_{\mathbf{z}}\,dz'}_{\overline{\mathbf{v}}_{\mathbf{rel}}} + \overline{\mathbf{v}}_{\mathbf{ref}}(z_l) \equiv \overline{\mathbf{v}}_{\mathbf{rel}}(z_u) + \overline{\mathbf{v}}_{\mathbf{ref}}(z_l) \tag{6}$$

Here the integral indicated with the underbrace, in combination with Eq. 5, is defined as the relative velocity v_{rel}. Also $\overline{\mathbf{v}}$ becomes the integral of $\overline{\mathbf{v}}_{\mathbf{z}}$ plus an integration constant, which needs to be a known reference velocity. Or equivalently, $\overline{\mathbf{v}}$ then consists of a depth-dependent relative velocity $\mathbf{v_{rel}}$ and a depth-independent reference velocity $\mathbf{v_{ref}}$. Inserting Eq. (6), into Eq. (4) leaves,

$$v_z^{\perp} = (\mathbf{v_{rel}} \cdot \boldsymbol{\tau})_z + \mathbf{v_{ref}} \cdot \boldsymbol{\tau_z}. \tag{7}$$

Vertically integrating this equation results in an expression for $v^{\perp}$,

$$[v^{\perp}]_{z_l}^{z_u} = [\mathbf{v_{rel}} \cdot \boldsymbol{\tau}]_{z_l}^{z_u} + \mathbf{v_{ref}} \cdot (\boldsymbol{\tau}(z_u) - \boldsymbol{\tau}(z_l)). \tag{8}$$

The relative velocity $\mathbf{v_{rel}}$ can be obtained from Θ, S_A and p fields alone. Methods to determine $\mathbf{v_{ref}}$ from data, or eliminate this term completely, will follow in Section 2c. In the next step we first show how to obtain the cross-contour velocity on the left hand side ($v^{\perp}$) as an expression with only the mixing coefficients K and D as unknowns.

b. Finding an expression for $v^{\perp}$ in terms of K and D

An equation that describes the cross-contour velocity as a function of the mixing coefficients K and D was first derived by McDougall (1984), who referred to this as the water-mass transformation equation. We however, use the form as described in IOC et al. (2010), with the difference being the K_{GM}-term. This term follows from parameterization of the quasi-Stokes velocity. The full derivation of the equation that will be used here, can be found in Appendix A:

$$\begin{aligned} v^{\perp} = & \frac{1}{|\nabla_n \hat{\Theta}|} \gamma_z \nabla_n \cdot \left(\gamma_z^{-1} K \nabla_n \hat{\Theta}\right) + \frac{1}{|\nabla_n \hat{\Theta}|} K g N^{-2} \hat{\Theta}_z \left(C_b^{\Theta} \nabla_n \hat{\Theta} \cdot \nabla_n \hat{\Theta} + T_b^{\Theta} \nabla_n \hat{\Theta} \cdot \nabla_n P\right) \\ & + \frac{1}{|\nabla_n \hat{\Theta}|} D \beta^{\Theta} g N^{-2} \left(\hat{\Theta}_z \hat{S}_{Azz} - \hat{S}_{Az} \hat{\Theta}_{zz}\right) - \left(\frac{K_{GM} \nabla_z \overline{\gamma}}{\overline{\gamma}_z}\right)_z \cdot \frac{\nabla_n \hat{\Theta}}{|\nabla_n \hat{\Theta}|} \end{aligned} \tag{9}$$

In this equation, γ_z is the vertical derivative of neutral density (γ^n) (Jackett and McDougall 1997). Here the first term on the right hand side is the isoneutral mixing. The second term is a result of non-linearities in the equation of state. That is, cabbeling and thermobaricity processes will cause a dianeutral motion due to isoneutral mixing along the neutral tangent plane (McDougall 1987b;

Klocker and McDougall 2010; Groeskamp et al. 2016). The third term accounts for the turbulent dianeutral mixing. The last term on the right hand side is the result of splitting the velocity into the Eulerian mean component and a fluctuating component that has been parameterized as the quasi-Stokes velocity. It can be argued that this K_{GM} should be taken as different from K (see e.g. Smith and Marshall (2009)), but, as in many studies of ocean circulation and mixing (Holmes et al. 2022), we here make the approximation that both coefficients are similar. In Equation (9), the only unknowns in the expression for the cross-contour velocity are the diffusivities ($v^{\perp} = [f(K,D)]$), while other terms can all be found using Θ, S_A and p data. There have been other studies that also used some form of Eq. (9) to infer the diffusivities. McDougall (1991) assumed a third conservative tracer equation to eliminate the advective terms from the equation. Zika et al. (2009) zonally integrated the equation along closed (circumpolar) tracer contours and found a ratio of the diapycnal and isopycnal diffusivities, D/K. Here we combine the assumptions above with Equations (8) and (9), this allows us to write the combination as:

$$[v^{\perp}]_{z_l}^{z_u} = [f(K,D)]_{z_l}^{z_u} = [\mathbf{v_{rel}} \cdot \boldsymbol{\tau}]_{z_l}^{z_u} + \mathbf{v_{ref}} \cdot (\boldsymbol{\tau}(z_u) - \boldsymbol{\tau}(z_l)). \tag{10}$$

Note that here all the terms in $f(K,D)$ can be obtained from hydrographic data, except for the unknown K and D coefficients. The relative velocity term on the right hand side can be determined using Equation (5), but the reference velocity term remains usually unknown or highly uncertain. In the next section, it will be discussed how the reference velocity can be obtained or eliminated from the equations.

c. Eliminating the unknown v_{ref}-term.

While the relative velocity $\mathbf{v_{rel}}$ can be determined using Equation (5), the reference velocity $\mathbf{v_{ref}}$ remains unknown. This is not a problem when one has knowledge of the reference velocity, for example from a data product (e.g. Gray and Riser (2014); Lebedev et al. (2007)) or through observations of a moored current meter in the area of interest. For this study, our goal is to entirely eliminate the reference velocity from the SIM (Equation (10)). This has the advantage that the inversion does not have to deal with the uncertainties related to finding such reference velocity. Therefore our approach is to carefully select the upper and lower depths (z_u, z_l respectively) between which the equation are being integrated. These 'pairs' of depths are being selected such that $\boldsymbol{\tau}(z_u) = \boldsymbol{\tau}(z_l)$, so that the term containing the reference velocity drops out of Eq. (10). Then, the only unknowns in Equation (10) are the diffusivities K and D, while the other terms can all be written in terms of the fields of Θ, S_A and p.

d. An expression for the SIM including structure functions

For the application of the SIM in this study, we make use of structure functions of the isopycnal and diapycnal diffusivities. Structure functions are a-priori determined vertical profiles for K and D, that we make dependent on only one unknown diffusion coefficient with which these profiles will be scaled. As a consequence of using structure functions, all pairs in one vertical profile are connected and combined. As such we have more equations available to solve for fewer unknowns. A downside to using structure functions is that more a-priori knowledge is required or that alternatively, the resolution with which we resolve the vertical structure of the diffusivities is reduced. The SIM can also operate without structure functions, but regardless, choices will still have to be made about vertical resolution of diffusivities and which pairs are suitable for estimating a diffusivity. We here derive the equations for the SIM, including the structure functions (because this will be used in Section 4), using $f_K(z) = \frac{K^{\text{struc}}(z)}{K^{\text{struc}}_{\text{max}}}$ and $f_D(z) = \frac{D^{\text{struc}}(z)}{D^{\text{struc}}_{\text{max}}}$. These are vertical profiles of $K\&D$ scaled by their maximum, to obtain structure functions for K and D respectively. With K^{inv} and D^{inv} being the unknown constants of the inverse method, we can write the estimated diffusivity as;

$$K^{\text{est}}(z) = K^{\text{inv}} f_K(z) \quad \text{and} \quad D^{\text{est}}(z) = D^{\text{inv}} f_D(z) \tag{11}$$

Reordering the terms of Equation (9) and applying the structure functions results in,

$$\begin{aligned} v^{\perp} =& K^{\text{inv}} \left[\frac{1}{|\nabla_n \hat{\Theta}|} \gamma_z \nabla_n \cdot \left(\gamma_z^{-1} f_K(z) \nabla_n \hat{\Theta} \right) \right. \\ &+ \frac{1}{|\nabla_n \hat{\Theta}|} f_K(z) g N^{-2} \hat{\Theta}_z \left(C_b^{\Theta} \nabla_n \hat{\Theta} \cdot \nabla_n \hat{\Theta} + T_b^{\Theta} \nabla_n \hat{\Theta} \cdot \nabla_n P \right) \\ &\left. - \left(f_K(z) \frac{\nabla_z \overline{\gamma}}{\overline{\gamma}_z} \right)_z \cdot \frac{\nabla_n \hat{\Theta}}{|\nabla_n \hat{\Theta}|} \right] + D^{\text{inv}} \left[\frac{1}{|\nabla_n \hat{\Theta}|} f_D(z) \beta^{\Theta} g N^{-2} \left(\hat{\Theta}_z \hat{S}_{Azz} - \hat{S}_{Az} \hat{\Theta}_{zz} \right) \right]. \end{aligned} \tag{12}$$

Here $f_K(z)$ and $f_D(z)$ are scaling factors between 0 and 1, based upon the used structure function. K^{inv} and D^{inv} are the diffusivities that will be estimated by the SIM and basically rescale the a-priori assumed structure to fit the observational data.

In the next section, we discuss the data products used, as well as the structure functions that we use for K and D.

3. Data

We choose to apply the SIM to a globally gridded climatology of hydrographical data. Annual means of in situ temperature and practical salinity data from the World Ocean Atlas 2018 (WOA18) (Locarnini et al. 2019; Zweng et al. 2019) gridded climatology are used. The data has a grid spacing of 1° with 102 vertical levels. The in situ temperature and practical salinity data are converted to Conservative Temperature (Θ) and Absolute Salinity (S_A) using the GSW software toolbox (McDougall and Barker 2011; IOC et al. 2010). Static stability of the data is reached by applying a vertical stabilization algorithm (Barker and McDougall 2017). Neutral density (γ^n) is calculated according to Jackett and McDougall (1997). The neutral gradients of Θ and S_A are calculated using the 'Vertical Non-local Method (VENM)' of Groeskamp et al. (2019).

When the neutral tracer gradients of Θ and S_A are known and regridded to WOA18 depths, the different terms of Equations (5) and (9) can be calculated. First and second vertical derivatives of Θ, S_A and γ^n are obtained using a second order vertical differences scheme and smoothed with a vertical 3 point running mean. Remaining small-scale oscillations are removed by applying a vertical 11 point running mean smoother to the final terms over a cast. No additional horizontal smoothing between casts is applied. The sensitivity of the final estimates to the amount of smoothing is explored in Appendix B1. The results are somewhat sensitive to this smoothing process, but not once the main spikes are removed.

Equation (12) shows the water-mass transformation equation at a given geographical location with the structure functions included. In this application of the SIM we use two data-based fields (latitude, longitude, depth) for K and D respectively, and calculate the structure functions $f_K(z)$ and $f_D(z)$ at each location from these fields. We will base the spatial variation of the isoneutral eddy diffusion coefficient K on the estimate of Groeskamp et al. (2020). The study of Groeskamp et al. (2020) provides a parameterization for the isoneutral eddy diffusion coefficient based upon mixing length theory (Prandtl 1925) and mean flow suppression theory (Ferrari and Nikurashin 2010) and the theory of vertical modes (LaCasce and Groeskamp 2020).

As a structure function for the dianeutral turbulent diffusion coefficient D we will use the product of De Lavergne et al. (2020). The product of De Lavergne et al. (2020) is a parameterization based on the turbulence production due to internal tides. De Lavergne et al. (2020) uses four different pathways to account for both near-field and far-field dissipation of internal tides.

4. Inversion

To test and showcase the SIM, we apply it to the region where also the North Atlantic Tracer Release Experiment (NATRE) took place (Ledwell et al. 1993). This region spans the area between $38° - 27°\ W$ and $21° - 29°\ N$ (red box, Fig. 1). Due to NATRE and subsequent studies, there are direct observations and indirect estimates of the mixing available for both K and D, that we can use to compare the SIM against (Section 6).

First we will focus on defining suitable combinations of depths, that is, locations where the second term on the right hand side of Equation (10) is approximately zero. After this we will discuss the several choices and considerations that have been made during the inversion process.

a. Finding combinations of z_u and z_l

Using the neutral gradients of Θ and S_A, the orientation of the contours τ on the neutral surfaces can be calculated using Equation (1). As described in Section 2.c, the reference velocity $\mathbf{v_{ref}}$ is eliminated by finding combinations of depths, where τ has the same orientation. We make the approximation that a difference of $\Delta\tau = \tau_u - \tau_l < 0.0075\ [rad]$ can be considered negligible and therefore both contours would have the same orientation. The choice for a certain $\Delta\tau$ does have impact on the amount of pairs that can be found as well as on the uncertainty of the estimates. All in all the SIM is not particularly sensitive to this choice and the choice of $crt = 0.0075\ [rad]$ is appropriate (Appendix B2).

This condition is calculated for all the different gridpoints within the study area. Starting at the surface, the difference $\Delta\tau$ is checked for all levels below. If the condition is met, that combination of depths can be used for the inversion. We will refer to all combinations of depths that meet the condition as 'pairs'. As air-sea fluxes are not (yet) included in the WMT equation (see also Appendix A), we only consider pairs that start below 300m depth, as this is below the maximum mixed layer depth in the area and below any incoming shortwave radiation (Groeskamp and Iudicone 2018). The incoming shortwave radiation can lead to significant watermass transformation rates not accounted for in Eq. 9.

The total depth integrated number of pairs for each gridpoint of WOA, that meet the criterium $\Delta\tau < 0.0075\ rad$, shows strong regional variation (Fig. 1). Note that this is before any selection is performed. In the study region (indicated by the red box) there is a relatively low number of suitable pairs when compared to some other areas around the world (e.g. the Southern Ocean). Yet, even within this small area there is significant variation in the amount of pairs left after applying the signal-to-noise criteria (Fig. 2).

For one gridpoint in the study area (marked with the red × in Fig. 2), the used signal-to-noise criteria were too strict (Section 4.c) and an insufficient number of pairs remained to obtain estimates for K and D. Most of the pairs found in the study area are concentrated between 1000m and 2000m, with especially limited number of pairs in the deeper parts of the watercolumn that remain after the signal-to-noise criteria (Fig.3). Even though the pairs are not evenly distributed over depth, the used structure functions (Section 2.d), link different pairs over the whole water column. That is, each pair will contribute to find the unknown diffusivity such that even for a low amount of pairs, or with an uneven vertical distribution, there will still be a full depth estimate of $K^{\text{est}}(z)$ and $D^{\text{est}}(z)$.

b. Applying structure functions to the equations

Equation (10) can be written for a large number of combinations of z_u and z_l, that meet the criteria $\boldsymbol{\tau}(z_u) = \boldsymbol{\tau}(z_l)$. All these equations can be combined to a system of equations of the form $\mathbf{A}\,\mathbf{x} = \mathbf{b}$. Here, $\mathbf{A}$ is a $N \times M$ matrix, with N being the number of combinations of an upper and lower depth, for which $\tau_u - \tau_l < 0.0075$. And M is the number of unknowns, which in this application is only K^{inv} and D^{inv}. Here $\mathbf{x}$ is a $M \times 1$ vector, containing the M unknown diffusivities. Finally, $\mathbf{b}$ is a $N \times 1$ vector containing the rhs of Equation (10) for each equation. Because $\boldsymbol{\tau}(z_u) = \boldsymbol{\tau}(z_l)$, the term containing the reference velocity thus drops out.

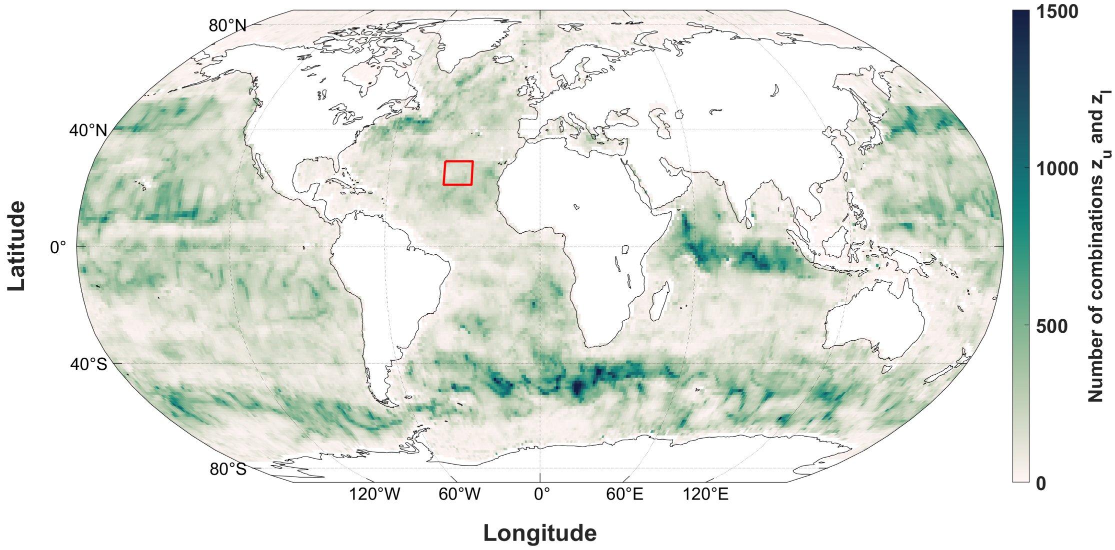

FIG. 1. Global distribution for the number of possible combinations between z_u and z_l, before any reduction based on signal-to-noise or other criteria. The study area of this paper is marked by the red box.

For the structure functions we use the geographical map of Groeskamp et al. (2020) for K and De Lavergne et al. (2020) for D. For each vertical cast (on a x,y grid) these values are scaled with their maximum value and used as described in Equation (12) and now included in the factors multiplying the unknowns in the matrix $\mathbf{A}$.

c. *Signal to noise criteria*

Before carrying out the inversion on the system of equations that follows from finding the pairs, the number of equations is reduced. Reducing the number of equations is done in order to avoid having one or a few equations, with a relatively large error, disturbing the estimate provided by the method. For example, an estimate of the order of magnitude of the unknowns can be obtained by dividing the $\mathbf{b}$-term by the terms in the $\mathbf{A}$-matrix. That is $K \approx \mathbf{b}/\mathbf{A}_K$ and $D \approx \mathbf{b}/\mathbf{A}_D$. If this initial estimate of K or D is already many order of magnitude larger or smaller than what can be expected for this area, we can conclude that the signal to noise ratio for this pair is too large. That is, if $\mathbf{A}$ is too small compared to $\mathbf{b}$, it holds no information and will only lead to noise.

To determine if an equation contains too much noise, we make use of existing estimates of mixing, i.e. we use the structure functions. The structure functions provide a reasonable estimate

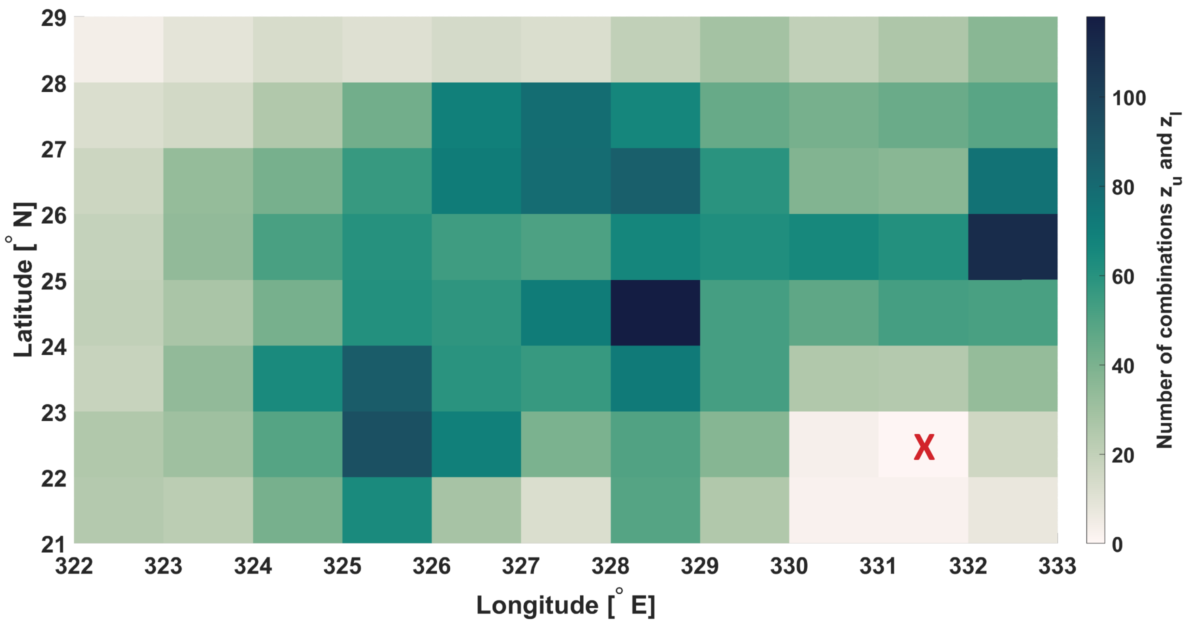

FIG. 2. The number of available pairs in the study area, after reduction based on the signal-to-noise criteria. For the red cross, insufficient pairs remain.

	D	K
Lower limit	$\max(1e^{-6}, D_{max}/10)$	$\max(25, K_{max}/10)$
Upper limit	$\min(5e^{-3}, 10 \cdot D_{max})$	$\min(5000, 10 \cdot K_{max})$

TABLE 1. The used lower and upper limits for the signal to noise criteria.

of the expected magnitude of K and D in this area. Although the actual K and D are unknown, these estimates can be used as a guideline. Hence, we use the maximum value from the structure function and assume that these are within a factor 10 of the actual K and the actual D. We also set minimum values under which we don't expect to be able to distinguish our results from zero. When the signal to noise value exceeds these boundaries (Table 1), we remove the equations.

Second, when either both terms in the A matrix are positive and the b term is negative, or vice versa, when both terms in the A matrix are negative and the b term is positive, it means that at least K or D, but possibly both, need to be negative. As the SIM is applied to annual-mean data, we assume that negative diffusivities are not physically realistic over such large timescales and remove related equations. Hence in these situations the data quality or the assumptions in the derivation, lead to an unphysical situation.

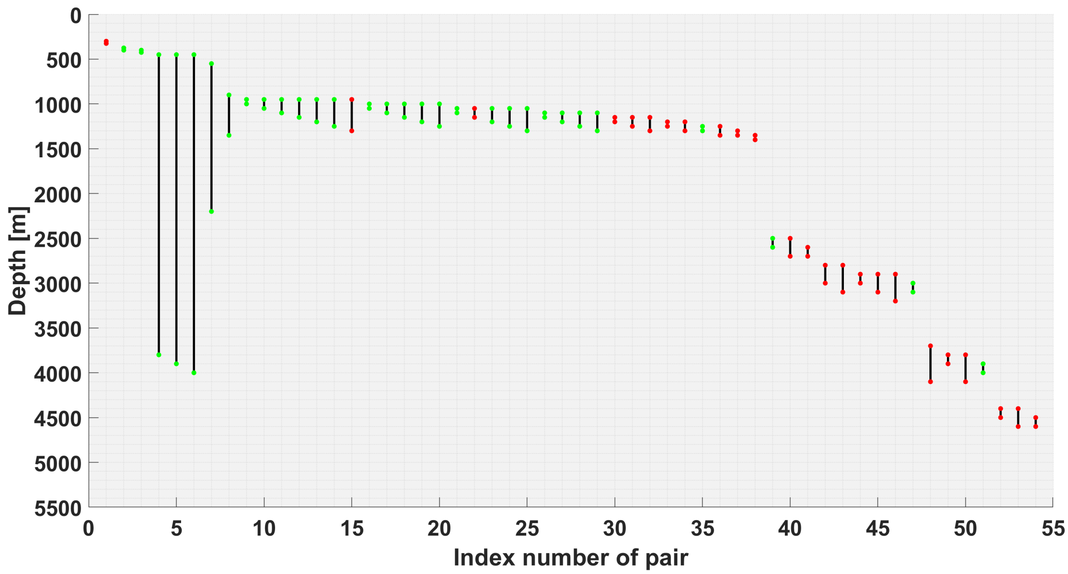

FIG. 3. Distribution of the pairs over the water column for a location in the study area. Pairs with red endpoints will be removed by the signal to noise criteria, pairs with green endpoints remain and are used for the inversion.

d. Solving for the unknowns

The data products used for estimating the diffusivities contain inaccuracies. Hence, for each equation there is equation error to minimize. Adding this to the system of equations ($\mathbf{A}\ \mathbf{x} = \mathbf{b}$) adds N values to minimize, to the M unknown variables to estimate. There are only N equations in the system, so the system is per definition underdetermined. An underdetermined system has infinite solutions (Wunsch 1978). Finding the solution can be done by minimizing χ^2, which is the sum of the equation errors and the solution error. It also provides a way of obtaining an error or sensitivity estimate of the solution. Here χ^2 is given by (McIntosh and Rintoul 1997; Menke 2018),

$$\chi^2 = (\mathbf{x} - \mathbf{x_0})^T \mathbf{W_c}^{-2} (\mathbf{x} - \mathbf{x_0}) + \mathbf{e}^T \mathbf{W_r}^2 \mathbf{e}. \tag{13}$$

$\mathbf{x_0}$ is an initial estimate for the unknowns, and the error $\mathbf{e}$ can be written as $\mathbf{e} = \mathbf{A}\mathbf{x} - \mathbf{b}$. A solution for $\mathbf{x}$ is found by minimizing χ^2:

$$\mathbf{x} = \mathbf{x_0} + \mathbf{W_c^2} \mathbf{A}^T \left(\mathbf{A} \mathbf{W_c^2} \mathbf{A^T} + \mathbf{W_r^{-2}} \right)^{-1} (\mathbf{b} - \mathbf{A}\mathbf{x_0}) \tag{14}$$

Here, $\mathbf{W_c}$ and $\mathbf{W_r}$ are the column and row weighting matrices. These matrices are diagonal with elements σ_x and $1/\sigma_e$. With that, Equation (14) can be rewritten to,

$$\begin{aligned}\chi^2 &= \chi_x^2 + \chi_e^2 \\ &= \sum_{m=1}^{M} \frac{(x_m - x_{0,m})^2}{\sigma_{x_m}^2} + \sum_{n=1}^{N} \frac{e_n^2}{\sigma_{e_n}^2}\end{aligned} \tag{15}$$

Equation (14) gives an estimate of $\mathbf{x}$ and an estimate of the random error in this estimate can be found using the posterior covariance matrix.

$$\mathbf{C_p} = \mathbf{W_c}^2 - \mathbf{W_c}^2\mathbf{A}^\mathbf{T}(\mathbf{A}\mathbf{W_c}^2\mathbf{A}^\mathbf{T} + \mathbf{W_r}^{-2})^{-1}\mathbf{A}\mathbf{W_c}^2 \tag{16}$$

The standard deviation of the estimates can then be obtained by taking the square root of the diagonal elements of the matrix $\mathbf{C_p}$ (McIntosh and Rintoul 1997).

e. Sensitivity analysis

The standard deviation of the estimates obtained from the posterior covariance matrix $\mathbf{C_p}$ is a statistical interpretation of the uncertainty of the method. However, this standard deviation may be physically unrealistic at the same time, and not fairly represent the sensitivity of the different variables that are subject to the modellers choices. This is especially the case when prior statistics are not well known (Groeskamp et al. 2014). We will follow the method used by Groeskamp et al. (2014) to obtain a physically realistic uncertainty estimate. We will vary the elements of the vector $\mathbf{x_0}$ (with elements D_0 and K_0, the initial guesses for D and K), σ_x (for both D and K) and σ_e. σ_x is our best guess for the error between $\mathbf{x_0}$ and $\mathbf{x}$. σ_e is our best guess for the equation error. We will vary each of these five variables over a range of values which we deem realistic and could all provide an equally true answer. These values are shown in Table 2.

By calculating χ_e^2 and χ_x^2 for all combinations of these five varying variables and selecting those for which $\chi_e^2 \approx N$ and $\chi_x^2 \approx M$, and for which the estimate for both K and D is positive (the influence of this constraint is analysed in App. C), we avoid fitting the final estimate to either the equations or to $\mathbf{x_0}$. This is done by taking the values for which,

Variable	Values
D_0	$D_{\max}^{\text{struc}} \cdot h_1, \text{with} \begin{Bmatrix} h_1 \in [0.1, 0.9],\ \Delta h_1 = 0.1 \\ h_1 \in [1, 10],\ \Delta h_1 = 1 \end{Bmatrix}$
K_0	$K_{\max}^{\text{struc}} \cdot h_2, \text{with} \begin{Bmatrix} h_2 \in [0.2, 0.8],\ \Delta h_2 = 0.2 \\ h_2 \in [1, 5],\ \Delta h_2 = 1 \end{Bmatrix}$
$\sigma_{x,D}$	$D_0 \cdot h_3, \text{with} \{h_3 \in [1, 10],\ \Delta h_3 = 1\}$
$\sigma_{x,K}$	$K_0 \cdot h_4, \text{with} \{h_4 \in [1, 10],\ \Delta h_4 = 1\}$
σ_e	$\overline{\lvert e_0 \rvert} \cdot h_5, \text{with} \begin{Bmatrix} h_5 \in [0.1, 1],\ \Delta h_5 = 0.1 \\ h_5 \in [1.5, 5],\ \Delta h_5 = 0.5 \\ h_5 \in [6, 10],\ \Delta h_5 = 1 \end{Bmatrix}$

TABLE 2. Used range of values for the variables used as sensitivity analysis. With $e_0 = \mathbf{b} - \mathbf{A}\mathbf{x_0}$. Note that after defining a-priori estimates of D_0 and K_0, the tested range for $\sigma_{x,D}$ and $\sigma_{x,K}$ are a function of this choice. The interval-width used to define D_0, K_0 and the σ-values are chosen such that the covered ranges (e.g. 0.1-1, or 1-10) all have approximately equal importance in the solution space.

$$\frac{N}{5} \leq \chi_e^2 \leq 5N \quad \text{and} \quad \frac{M}{5} \leq \chi_x^2 \leq 5M \tag{17}$$

Following this procedure leads to a set of values of K and D that are physically realistic. The values for K^{inv} and D^{inv} are taken to be the median of this set. In Figures 6 and 7, the variation in estimates by this sensitivity analysis is marked by the 25$^{\text{th}}$ and 75$^{\text{th}}$ percentile values. Respectively, the range spanned by the 25$^{\text{th}}$ and 75$^{\text{th}}$ percentiles (average over the study area) is between 782 $[m^2/s]$ and 1026 $[m^2/s]$ for K^{inv}, and 9.8×10^{-5} $[m^2/s]$ and 3.5×10^{-4} $[m^2/s]$ for D^{inv}. Whereas the standard deviation provided by the posterior covariance method gives an average uncertainty of ± 1.5 $[m^2/s]$ for K^{inv} and $\pm 5 \times 10^{-7}$ $[m^2/s]$ for D^{inv}.

As a test, we also solve the system using the formally overdetermined problem $\mathbf{A}\ \mathbf{x} = \mathbf{b}$, without the addition of weights and prior estimates of x. The results are found to be close to the estimates from our method described in section 4, though the over-determined problem does occasionally find negative estimates (Table 3). As outlined above, the negative results are considered mathematically valid, though not physically realistic.

The general agreement between the results give confidence that overall the theoretical model works, while the occasional negative results argue for guiding the inverse method to obtain the physically realistic estimates (e.g., by varying $\mathbf{x_0}$, and the row and column weights) of the solution space. We will further discuss the results of the study area in Section 5.

Location	**Estimates D** 25th percentile	(All values $\times 10^{-4}$) Median	75th percentile	A\b	**Estimates K** 25th percentile	Median	75th percentile	A\b
(330E, 27N)	2,46	3,32	3,69	3,67	1062	1152	1194	1192
(324E, 24N)	1,20	1,61	1,79	1,63	949	994	1011	997
(333E, 22N)	0,12	0,31	0,47	0,44	1224	1530	1897	1389
(331E, 23N)	0,06	0,16	0,50	−2,29	1199	1915	2890	−600
(332E, 27N)	0,47	1,17	2,20	−3,19	657	679	711	558

TABLE 3. Estimates for 5 random locations in the study area as shown by the median value and $25^{th}/75^{th}$ percentile values and the estimates obtained by solving the formally overdetermined problem A\b.

5. Results - Application of the SIM to a region in the Northern Atlantic

Following the steps as outlined in Section 4, results in an estimate for K^{inv} and D^{inv} through performing an inversion for each gridpoint in the study area. As outlined, the values presented for K^{inv} and D^{inv} are the median values found in the sensitivity analysis. The averaged (over the study area) median values are 917 $[m^2/s]$ for K^{inv} (full range of the sensitivity study is $0-8101$ $[m^2/s]$) and 2×10^{-4} $[m^2/s]$ for D^{inv} (full range of the sensitivity study is $5.9\times10^{-11}-1\times10^{-2}$ $[m^2/s]$). Note that the full range gives the ends of a narrow, longtailed distribution.

We find that K^{inv} shows a larger spread and a different spatial distribution than $K^{\text{struc}}_{\text{max}}$ (Fig. 4). The maximum value for K^{inv} is with a value of 2239 $[m^2/s]$ about a factor three larger than the maximum value for the structure function $(1194\ [m^2/s])$ in this study area. Though the maximum for K^{inv} might be considered an outlier, it is not an unrealistic high value. For D (Fig. 5), the spread of the values for D^{inv} is about the same order of magnitude when compared to the values for $D^{\text{struc}}_{\text{max}}$. A different spatial distribution can be observed in the figure. Note that an exact match with the structure functions, both in magnitude and spatial distribution, is not required. Instead, the SIM indicates that, when we look at the balance of Eq. (10), which includes both K and D, this is only possible to fullfill when both the values of K and D are altered a bit compared to the original structure functions as shown in Eq. (12). The structure functions themselves are independent estimates of K and D, not accounting for any such balance. The estimates for K are generally within a factor 2 or 3 from the original structure function. Which is arguably also within the range of uncertainty that such estimates currently have. A similar argument could be made for estimates of D that are mostly within an order of magnitude from the original structure function. Even the best estimates of D (e.g., from a vertical microstructure profiler) are only accurate within a factor 2 at most (Oakey 1982). In Figure 6 we explore in more detail the accuracy of the inverse estimates and the difference with the structure function. We find that the inverse estimates of K (with uncertainty estimate from the χ-criteria of Section (4)) tend to be at most a factor 4 different from the structure function, while mainly staying within a factor 3. For D, the values for both $D_{\text{max}}^{\text{struc}}$ and D^{inv} range from $10^{-5} - 10^{-3}$ $[m^2/s]$, which are common values for the dianeutral mixing coefficient. Most estimates fall within a factor 5 from the corresponding values for $D_{\text{max}}^{\text{struc}}$. And even with the uncertainty estimate provided based upon the χ-criteria from Section (4), the estimates are well within the range of what can be considered acceptable.

The results indicate that for estimates of D^{inv}, a larger maximum value of the structure function, also provides a larger estimate of D^{inv}, while this is not the case for estimates of K^{inv}. Especially for lower values of $K_{\text{max}}^{\text{struc}}$, there is a large spread in values of K^{inv}. Fig. 4a shows that these values can mostly be found on the northern side of the study area. Fig. 2 shows that these are also the casts for which only a limited number of equations remain after the signal to noise criteria. This indicates that with a lower number of equations the results are possibly more sensitive to noise, or that the pairs in this region themselves contain more noise.

The SIM and the two structure functions are three ways to obtain estimates, that all have their own assumptions and limitations. The fact the estimates for K and D are close to those of the structure functions indicates that the SIM has skill to estimate diffusion coefficients from observations and can help to constrain mixing parameterization theories with observations. Note that the influence of using different structure functions (see App. D) shows that, even though the shape is retained by construction, the magnitude can vary strongly if required by the balance that we are estimating. We conclude that while the selection of the structure function has influence on the final solution, the additional constraints of the SIM provide new information that can improve the existing estimates of K and D.

6. Comparing to different studies

After averaging all profiles of $K^{\text{est}}(z)$ and $D^{\text{est}}(z)$ (see Eq. (11)) over the study area, we can compare it against other studies (Fig. 7). We find that the SIM compares well against diffusivities obtained from direct observations (in black) or indirect estimates (in color).

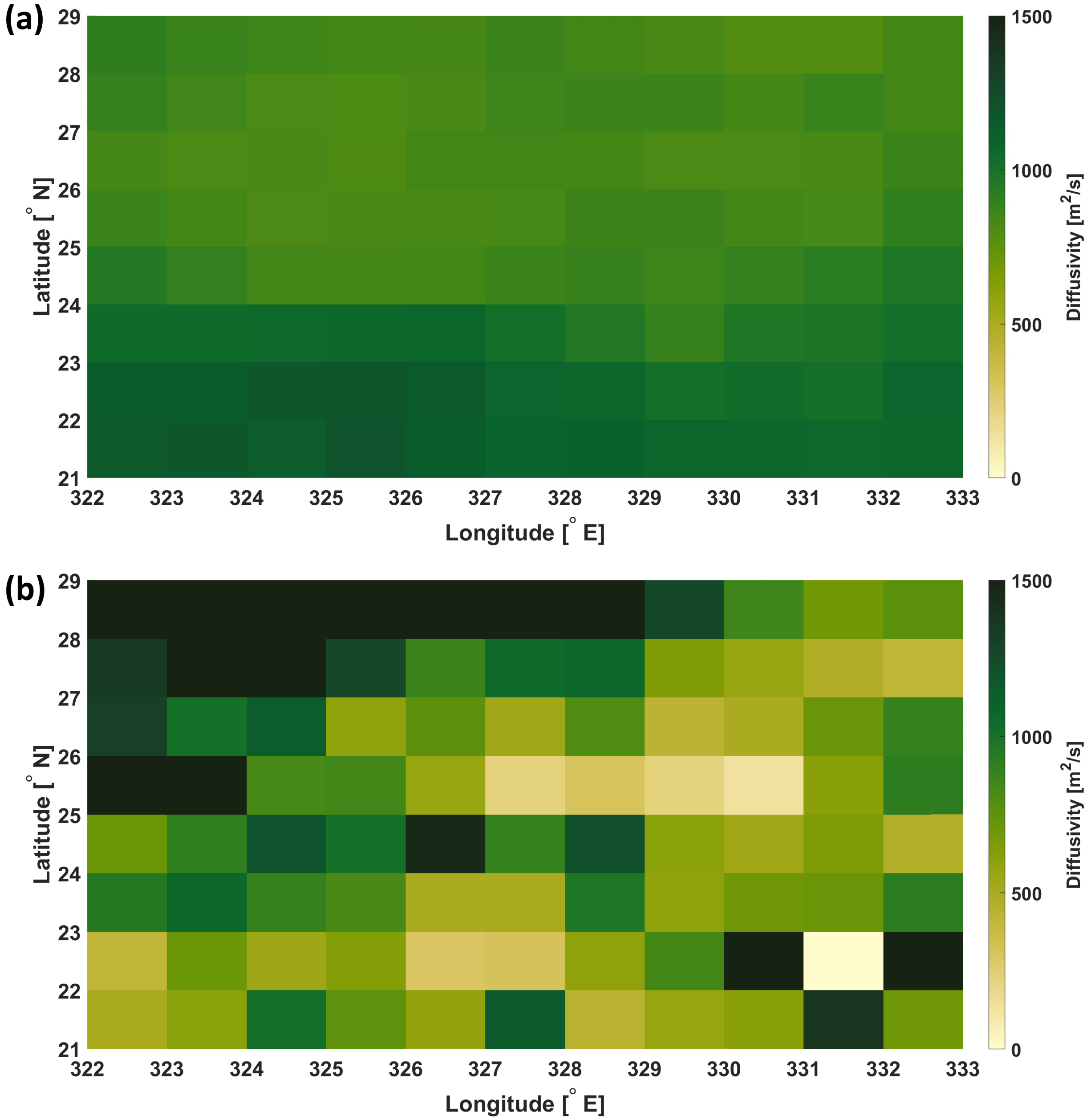

FIG. 4. The values for (a) $K^{\text{struc}}_{\text{max}}$ and (b) K^{inv} in the study area.

The dianeutral diffusivity D (Fig. 7, (a)), overlaps with both previous estimates as well as direct observations, even though the median is on the larger end of other estimates. Especially when including the uncertainty range of the SIM (red background shading, which is somewhat distorted due to the logarithmic scaling). The direct observations consist of microstructure profiles (Toole

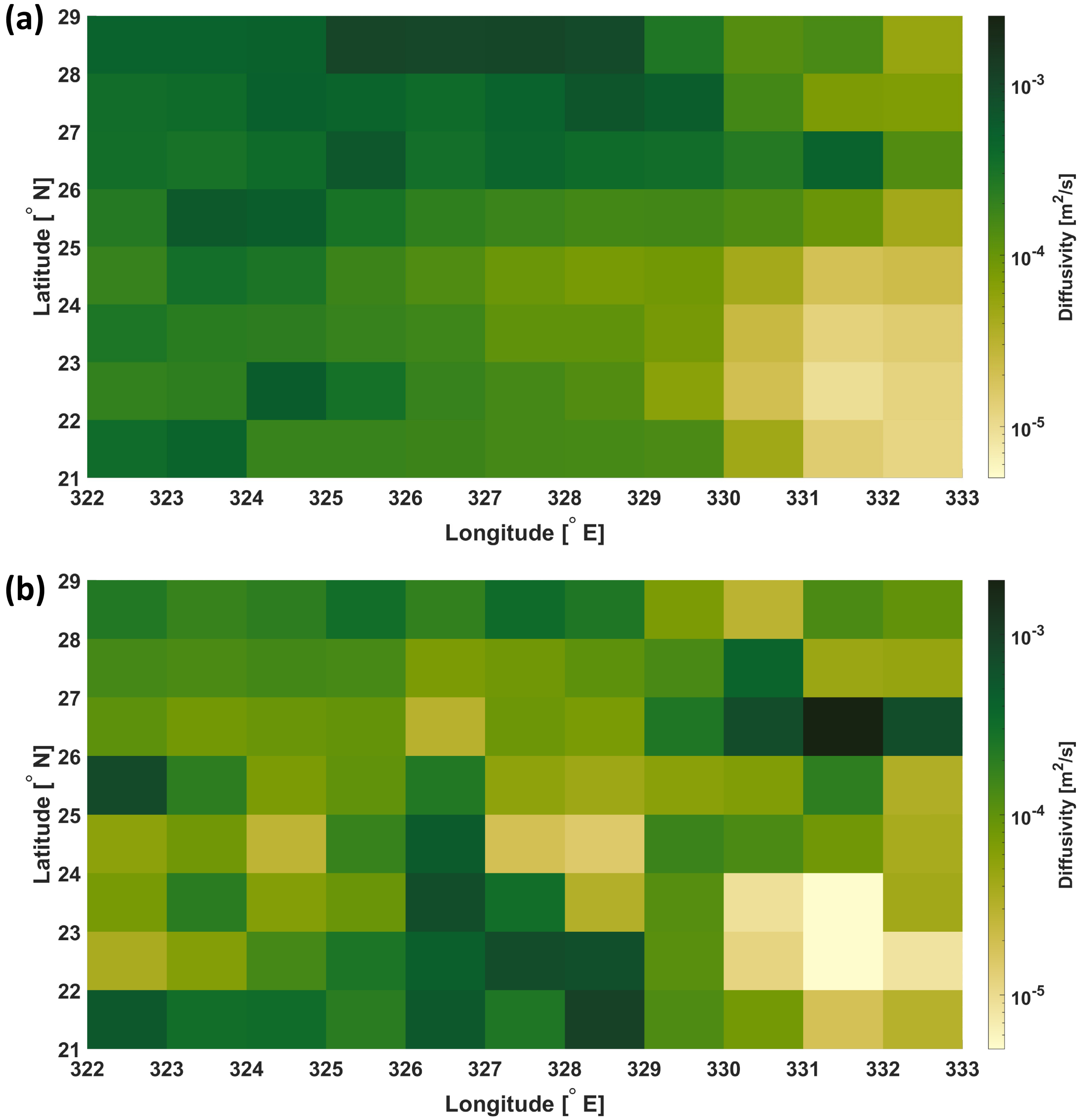

FIG. 5. The values for (a) $D^{\mathrm{struc}}_{\mathrm{max}}$ and (b) D^{inv} in the study area.

et al. 1994) and the vertical spread of a released tracer (Ledwell et al. 1998). The indirect estimates are the Tracer Contour Inverse Method (Zika et al. 2010b), estimates based on internal wave energy (De Lavergne et al. 2020) (upon which the structure function is based), and based upon the application of the finescale parameterization to Argo data (Whalen et al. 2018). The uncertainty

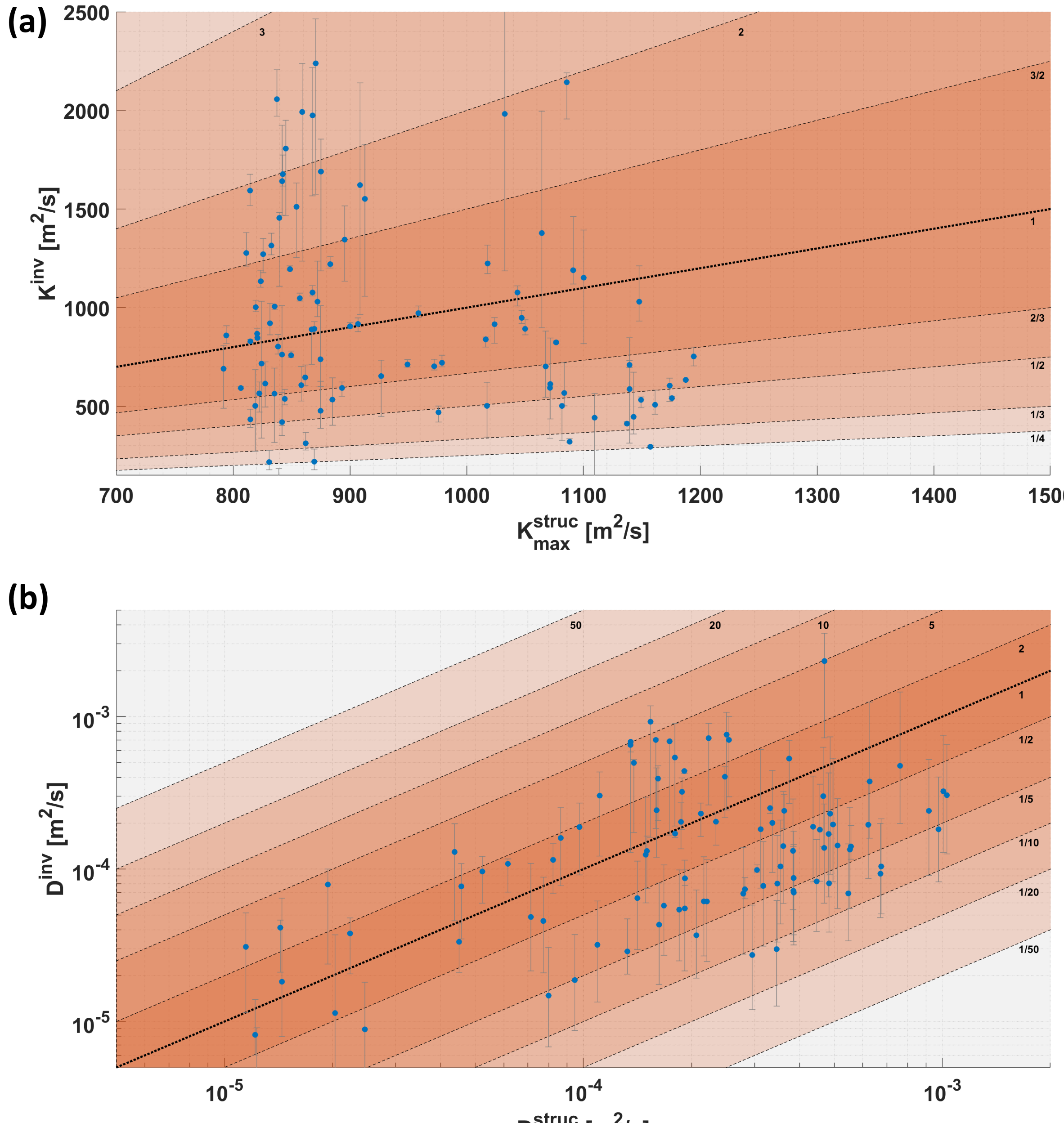

FIG. 6. The inverse estimates (blue dots) for (a) K^{inv} and (b) D^{inv} plotted against the value of the used structure functions. The orange shading represents the ratio between estimated value and the value of the structure function. Gray lines mark the uncertainty of the estimate, given by the 25^{th} and 75^{th} percentiles.

range provided by the SIM compares well to the variability as shown by the microstructure data (e.g, between 2700 and 3000 meters depth). Note that for all these studies, the timescales over which these small-scale mixing measurements are taken, or estimates are made, vary largely. For example, the microstructure measurements provide an instantaneous observation, while the tracer experiment is an average over many months.

The average profile of the isoneutral diffusivity K compares well with the available direct observations (in black), and does not differ much from the structure function used. The estimate provided by Cole et al. (2015), seems to be overestimating the diffusivity in this region, while the inverse estimates of Thermohaline Inverse Method (THIM) of Groeskamp et al. (2017) and Tracer Contour Inverse Method (TCIM) of Zika et al. (2010b) are underestimates compared to the observations. One possible explanation for the difference between these methods, is the scale or region that is considered. The THIM is a global estimate, while the TCIM provides regional estimates. Instead, the SIM provides a balance that obtains quasi-local estimates of the diffusivities for scales larger than the Rossby radius (due to the use of the geostrophic balance). Also note that when different structure functions are used (App. D), the SIM does find different estimates. For example, with the study of Cole et al. (2015) as structure function, the SIM lowers the estimate compared to the structure function. This shows that the SIM is capable of finding a physically realistic estimate and is not restricted too much to the original magnitude of the structure functions.

7. Discussion and conclusions

We here introduced the Spiralling Inverse Method, a new inverse method for estimating the isoneutral and dianeutral mixing coefficients K and D, respectively. It does so by relating the watermass transformation equation to the thermal wind balance. It is the first inverse method designed for estimating the mixing strength that does not require estimates of velocities or streamfunctions of any kind. We here applied it to a small region in the North Atlantic to showcase its potential, which is discussed below, together with the caveats.

The SIM was applied to the hydrographic data from WOA18. The observational data included in WOA18 has been averaged horizontally, which introduced additional mixing in the results, as opposed to averaging on neutral surfaces. For now, this will influence the results in an unknown way. This additional mixing can be avoided by using neutrally averaged data when such data products become available. In this application of the SIM, we have omitted equations from the upper 300m, as the current form of the SIM does not include air-sea fluxes. Although this can be

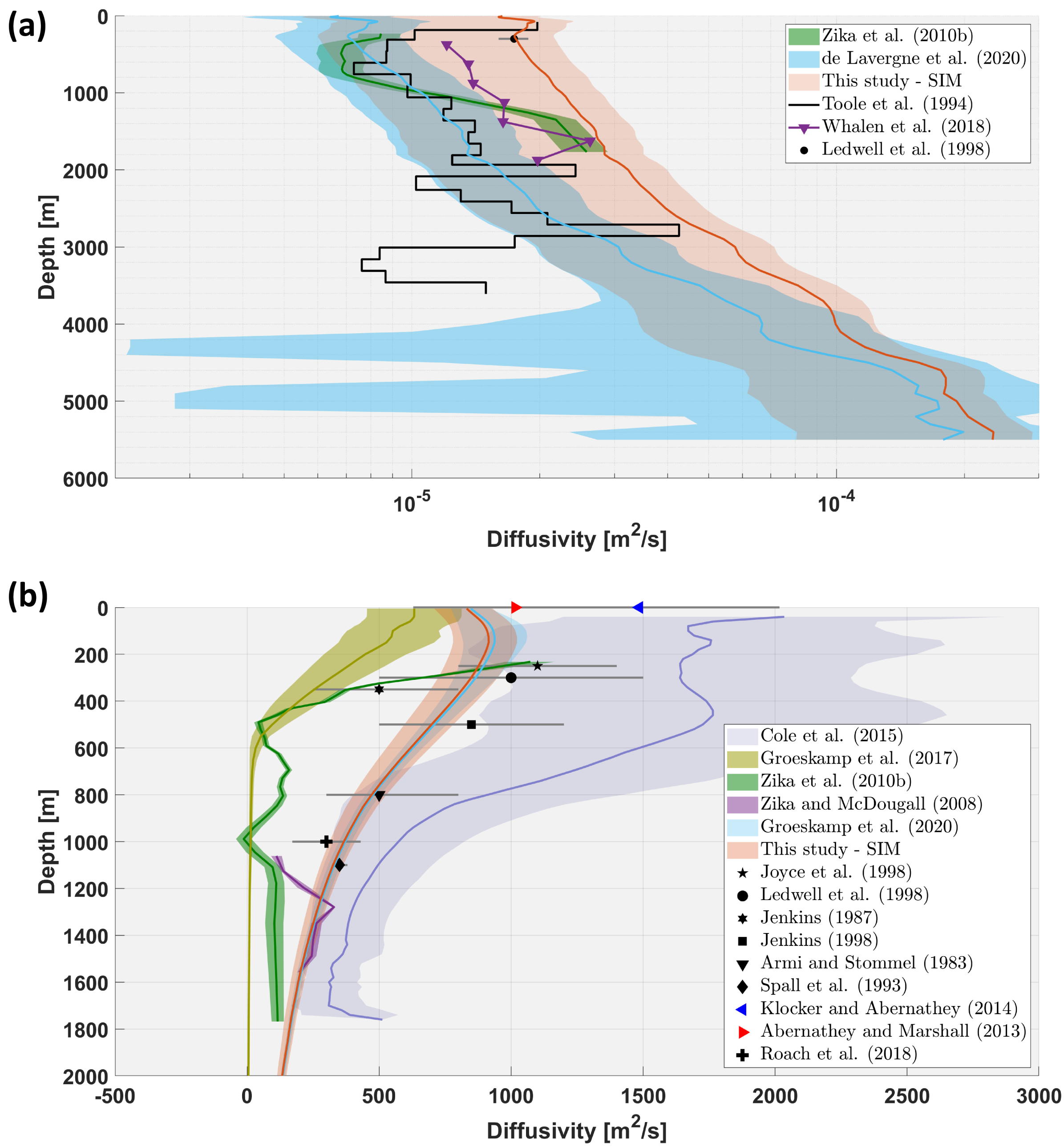

FIG. 7. Mean of the estimates of the SIM (in red) compared to other studies. Colored shadings mark the uncertainty of the corresponding study (colored solid lines). The uncertainty of the SIM is given by the average of 25^{th} and 75^{th} percentiles, With (a) the diapycnal estimate compared to (in black) direct observations (Toole et al. 1994; Ledwell et al. 1998) and (in color) indirect estimates (Zika et al. 2010b; De Lavergne et al. 2020; Whalen et al. 2018), and (b) the isopycnal estimate compared to (in black) direct observations (Joyce et al. 1998; Ledwell et al. 1998; Jenkins 1987, 1998; Armi and Stommel 1983; Spall et al. 1993; Roach et al. 2018) and (in color) indirect estimates (Cole et al. 2015; Groeskamp et al. 2017; Zika et al. 2010b; Zika and McDougall 2008; Groeskamp et al. 2020; Klocker and Abernathey 2014; Abernathey and Marshall 2013).

added in both the theory (see App. A) and the data, air-sea fluxes are known to cause large errors in WMT estimates (Groeskamp and Iudicone 2018) and may not improve the results, even when more equations are added as a result. Hence we choose to present the SIM without air-sea fluxes.

Although overlapping pairs of the SIM would contribute to provide multiple equations to estimate the unknowns, many pairs do only overlap over small ranges of depths (Fig. 3). Consequently we here used a structure function of the vertical shape of the diffusivities, which has the following advantages:

- It connects all pairs to estimate fewer unknowns.
- It provides an estimate where pairs do not exist.
- It provides a-priori information.

The caveat is that the result has fewer degrees of freedom and is more pre-determined by the chosen structure function. In future work, these structure functions can perhaps be less restrictive by adding more degrees of freedom, such that the mixing estimates are more determined by the data rather than the structure function. At the moment, the pairs that form the basis of the inversion are found based upon two important criteria; the first is the accuracy with which we want to satisfy the criterium $\tau_u - \tau_l \approx 0$, this was explored in App. B. It turns out that the SIM is not very sensitive to this choice, though one needs to be careful by not making this too strict or wide. The second criterion is related to the depth resolution at which the WOA-data is provided. When interpolating WOA onto different depths, or using a different dataset it might be possible to find more and more accurate pairs. More equations (information) could be obtained when more pairs are found with an increased vertical resolution of the dataset or when the reference velocity is included. However, that is with the caveat that the reference velocity might introduce another source of error.

The application of the SIM in this study, results in estimates of K and D that are within a realistic range from other estimates and observations of these diffusivities. This provides confidence in the potential for the SIM to be more widely used, possibly in combination with other inverse estimates. This could result in global inverse estimates of mixing and potentially observational based constraints for new and improved mixing parameterizations in (ocean) models. Thus reducing the uncertainty associated with the parameterizations and model outcomes.

Acknowledgments. This publication is supported by the project "Measuring the immeasurable: mapping of ocean mixing" with project number OCENW.M20.196 of the research programme Open Competition Domain Science (ENW) which is financed by the Dutch Research Council (NWO). This publication is supported by the project "The intermittency of large-scale ocean mixing" with project number 2020.3 financed by the Utrecht University and NIOZ research collaboration fund. T. McD gratefully acknowledges support from the Australian Research Council through grant FL150100090.

The authors thank two anonymous reviewers whose comments helped improve the manuscript.

Data availability statement. World Ocean Atlas data can be downloaded from `https://www.ncei.noaa.gov/access/world-ocean-atlas-2018/`

The mixing estimates presented in this manuscript are available as DOI:10.25850/nioz/7b.b.gh.

APPENDIX A

Watermass Transformation Equation

Here we derive the Water Mass Transformation equation as it is used in Section 2. The starting point are the conservation equations for Conservative Temperature Θ and Absolute Salinity S_A (see e.g. (IOC et al. 2010; McDougall 1984)).

$$\hat{\Theta}_{t|n} + \hat{\mathbf{v}} \cdot \nabla_n \hat{\Theta} + \tilde{e}\hat{\Theta}_z = \tilde{\gamma}_z \nabla_n \cdot \left(\tilde{\gamma}_z^{-1} K \nabla_n \hat{\Theta}\right) + \left(D\hat{\Theta}_z\right)_z \tag{A1a}$$

$$\hat{S}_{At|n} + \hat{\mathbf{v}} \cdot \nabla_n \hat{S}_A + \tilde{e}\hat{S}_{Az} = \tilde{\gamma}_z \nabla_n \cdot \left(\tilde{\gamma}_z^{-1} K \nabla_n \hat{S}_A\right) + \left(D\hat{S}_{Az}\right)_z + \hat{S}^{S_A} \tag{A1b}$$

$\hat{\Theta}$ and $\hat{S}_A$ are thickness-averaged Conservative Temperature and Absolute Salinity (the thickness-averaging being marked by the ˆ) and $\hat{\mathbf{v}}$ is the thickness-weighted velocity. $\tilde{e}$ is the dianeutral velocity temporally averaged on a neutral surface (the temporal average being marked by the ˜). Because unresolved motions in ocean models are assumed to move along locally referenced potential density surfaces, the temperature and salinity variables in ocean models are best interpreted as being the thickness-weighted averages where the averaging is done between pairs of locally defined potential density surfaces (McDougall and McIntosh 2001), with the thickness between successive surfaces being part of the averaging procedure. The last term in the conservation equation for

Absolute Salinity $\hat{S}_A$ is an additional source term because Absolute Salinity is not completely conserved (IOC et al. 2010). For our purposes this term is negligible since the isoneutral gradient of the difference between Absolute Salinity and Preformed Salinity is less than a percent of the isoneutral gradient of Absolute Salinity (Pawlowicz et al. 2012; IOC et al. 2010). This implies that the diffusivities (either K or D) that are needed to balance these isoneutral gradients would be different by less than one percent. The vertical gradients of the difference between these salinity variables is also very small, particular in the North Atlantic.

In this current derivation of the watermass transformation equation air-sea fluxes have not been included. At the sea surface the air-sea heat (Groeskamp and Iudicone 2018) and salt fluxes (Nurser and Griffies 2019) take the place of the parameterized diapycnal mixing terms in Eqs. (A1a) and (A1b) (IOC et al. 2010). Including air-sea fluxes in the SIM is left for future work.

Multiplying Equation (A1a) with the thermal expansion coefficient α and Equation (A1b) with the saline contraction coefficient β, followed by substracting Equation (A1b) from Equation (A1a) results in,

$$\begin{aligned}\underbrace{\alpha\hat{\Theta}_t|_n-\beta\hat{S_{A}}_t|_n}_{=0}+\hat{\mathbf{v}}\underbrace{(\alpha\nabla_n\hat{\Theta}-\beta\nabla_n\hat{S}_A)}_{=0}+\widetilde{e}\underbrace{(\alpha\hat{\Theta}_z-\beta\hat{S_{A}}_z)}_{=g^{-1}N^2}=\\ \alpha\widetilde{\gamma}_z\nabla_n\cdot(\widetilde{\gamma}_z^{-1}K\nabla_n\hat{\Theta})-\beta\widetilde{\gamma}_z\nabla_n\cdot(\widetilde{\gamma}_z^{-1}K\nabla_n\hat{S}_A)+\alpha(D\hat{\Theta}_z)_z-\beta(D\hat{S_{A}}_z)_z-\beta\hat{S}^{S_A}.\end{aligned} \tag{A2}$$

Note that on a neutral plane the following relations hold: $\alpha\nabla_n\hat{\Theta}-\beta\nabla_n\hat{S}_A=0$ and $\alpha\hat{\Theta}_t|_n-\beta\hat{S}_{A_t}|_n=0$ (McDougall 1987a), and the definition of the buoyancy frequency: $g^{-1}N^2=(\alpha\Theta_z-\beta S_{A_z})$ (McDougall 1987a). These reduce the equation above to an expression for the dianeutral velocity;

$$\widetilde{e}g^{-1}N^2=\alpha\widetilde{\gamma}_z\nabla_n\cdot(\widetilde{\gamma}_z^{-1}K\nabla_n\hat{\Theta})-\beta\widetilde{\gamma}_z\nabla_n\cdot(\widetilde{\gamma}_z^{-1}K\nabla_n\hat{S}_A)+\alpha(D\hat{\Theta}_z)_z-\beta(D\hat{S}_{A_z})_z-\beta\hat{S}^{S_A} \tag{A3}$$

We use the following definitions for the cabbeling and thermobaricity parameters (IOC et al. 2010),

$$C_b = \left.\frac{\partial \alpha}{\partial \hat{\Theta}}\right|_{\hat{S}_A,p} + 2\frac{\alpha}{\beta}\left.\frac{\partial \alpha}{\partial \hat{S}_A}\right|_{\hat{\Theta},p} - \left(\frac{\alpha}{\beta}\right)^2 \left.\frac{\partial \beta}{\partial \hat{S}_A}\right|_{\hat{\Theta},p} \tag{A4a}$$

$$\text{and} \quad T_b = \left.\frac{\partial \alpha}{\partial P}\right|_{\hat{S}_A,\hat{\Theta}} - \frac{\alpha}{\beta}\left.\frac{\partial \beta}{\partial P}\right|_{\hat{S}_A,\hat{\Theta}} \tag{A4b}$$

and combine these with Equation (A3), to obtain,

$$\widetilde{e} g^{-1} N^2 = -K\left(C_b \nabla_n \hat{\Theta}\cdot\nabla_n \hat{\Theta} + T_b \nabla_n \hat{\Theta}\cdot\nabla_n P\right) + \alpha(D\hat{\Theta}_z)_z - \beta(D\hat{S}_{A_z})_z - \beta\hat{S}^{S_A} \tag{A5}$$

Rewriting Equation (A5) results in,

$$(\widetilde{e} - D_z)\, g^{-1} N^2 = -K\left(C_b \nabla_n \hat{\Theta}\cdot\nabla_n \hat{\Theta} + T_b \nabla_n \hat{\Theta}\cdot\nabla_n P\right) + D\left(\alpha\hat{\Theta}_{zz} - \beta\hat{S}_{Azz}\right) - \beta\hat{S}^{S_A} \tag{A6}$$

Substituting Equation (A6) into Equation (A1a), and reordering the terms gives,

$$\begin{aligned}\hat{\Theta}_{t|n} + \hat{\mathbf{v}}\cdot\nabla_n\hat{\Theta} = \tilde{\gamma}_z \nabla_n\cdot\left(\tilde{\gamma}_z^{-1} K \nabla_n \hat{\Theta}\right) + KgN^{-2}\hat{\Theta}_z\left(C_b \nabla_n \hat{\Theta}\cdot\nabla_n \hat{\Theta} + T_b \nabla_n \hat{\Theta}\cdot\nabla_n P\right) \\ -DgN^{-2}\hat{\Theta}_z\left(\alpha\hat{\Theta}_{zz} - \beta\hat{S}_{Azz}\right) + D\hat{\Theta}_{zz} + \frac{\beta}{\alpha}\frac{R}{R-1}\hat{\mathbf{S}}^{S_A},\end{aligned} \tag{A7}$$

where $R = \frac{\alpha\hat{\Theta}_z}{\beta\hat{S}_{Az}}$.

The two diapycnal mixing terms in the equation above can be merged to get either

$$\begin{aligned}-DgN^{-2}\hat{\Theta}_z\left(\alpha\hat{\Theta}_{zz} - \beta\hat{S}_{Azz}\right) + D\hat{\Theta}_{zz} &= D\beta gN^{-2}\hat{\Theta}_z^3\frac{d^2\hat{S}_A}{d\hat{\Theta}^2} \\ &= D\beta gN^{-2}\left(\hat{\Theta}_z\hat{S}_{Azz} - \hat{S}_{Az}\hat{\Theta}_{zz}\right)\end{aligned} \tag{A8}$$

With the assumption of a steady state, the first term of Equation (A7) $\hat{\Theta}_{t|n}$ can be ignored. The last term on the rhs. in (A7), which reflects that Absolute Salinity is not conserved, is small and will be ignored (IOC et al. 2010). This results in,

$$
\begin{aligned}
\hat{\mathbf{v}}\cdot\nabla_n\hat{\Theta} = \tilde{\gamma}_z\nabla_n\cdot\left(\tilde{\gamma}_z^{-1}K\nabla_n\hat{\Theta}\right) + KgN^{-2}\hat{\Theta}_z\left(C_b\nabla_n\hat{\Theta}\cdot\nabla_n\hat{\Theta} + T_b\nabla_n\hat{\Theta}\cdot\nabla_n P\right) \\
+D\beta gN^{-2}\left(\hat{\Theta}_z\hat{S}_{Azz} - \hat{S}_{Az}\hat{\Theta}_{zz}\right).
\end{aligned}
\tag{A9}
$$

Now the thickness-weighted mean horizontal velocity $\hat{\mathbf{v}}$ will be replaced in favour of the Eulerian-mean horizontal velocity. When this is done, the thickness-weighted mean horizontal velocity $\hat{\mathbf{v}}$ is decomposed into the Eulerian-mean horizontal velocity and the quasi-Stokes horizontal velocity: $\hat{\mathbf{v}} = \overline{\mathbf{v}} + \mathbf{v}^{+}$. The quasi-Stokes velocity $\mathbf{v}^{+}$ can be parameterized by the vertical derivative of the quasi-Stokes streamfunction (McDougall and McIntosh 2001):

$$
\mathbf{v}^{+} = \Psi_z = \left(-\frac{\overline{v'\gamma'}}{\overline{\gamma}_z} + \frac{\overline{v}_z}{\overline{\gamma}_z}\frac{\overline{\phi}}{\overline{\gamma}_z}\right)_z \tag{A10}
$$

In this equation, $\overline{\phi} \equiv \frac{1}{2}\overline{(\gamma')^2}$, is half the density variance at height z (McDougall and McIntosh 2001). The quasi-Stokes streamfunction can also be considered as the product of the eddy diffusivity (written as K_{GM}) and the neutral slope (Gent et al. 1995; Griffies 1998). For the definition of the neutral tangent plane we take $\boldsymbol{S} = (S_x, S_y) \equiv \nabla_n z = -\frac{\nabla_z\overline{\gamma}}{\overline{\gamma}_z}$.

$$
\begin{aligned}
\Psi_z &= \left(\frac{K_{GM}\nabla_z\overline{\gamma}}{\overline{\gamma}_z}\right)_z \\
&= (K_{GM})_z\,\boldsymbol{S} - K_{GM}\left(\frac{\partial\boldsymbol{S}}{\partial z}\right) \\
&= (K_{GM})_z\,\boldsymbol{S} - K_{GM}\nabla_n\log\overline{\gamma}_z^{-1}
\end{aligned}
\tag{A11}
$$

To get from the second line of Eq. (A11) to the third line, we can write the vertical derivative of the slope as $-\boldsymbol{S}_z = \frac{(\nabla_z\overline{\gamma})_z}{\overline{\gamma}_z} - \frac{\overline{\gamma}_{zz}}{\overline{\gamma}_z}\frac{\nabla_z\overline{\gamma}}{\overline{\gamma}_z}$. This can be shown , in combination with Equation (10a) of McDougall et al. (2014), to be $\frac{(\nabla_z\overline{\gamma})_z}{\overline{\gamma}_z} - \frac{\overline{\gamma}_{zz}}{\overline{\gamma}_z}\frac{\nabla_z\overline{\gamma}}{\overline{\gamma}_z} = -\overline{\gamma}_z\nabla_z(1/\overline{\gamma}_z) - \overline{\gamma}_z\boldsymbol{S}(1/\overline{\gamma}_z)_z = -\nabla_n\ln(1/\overline{\gamma}_z)$.

In order to be completely correct, one should besides the quasi-Stokes velocity also account for the differences between thickness-weighted temperature and salinity and the Eulerian mean temperature and salinity: $\hat{\Theta} = \overline{\Theta} + \Theta^{+}$ and $\hat{S}_A = \overline{S}_A + S_A^{+}$. However, where the quasi-Stokes velocity can be parameterized following Eq. A10, to our knowledge no such parameterizations for Θ^{+} and S_A^{+} currently exist. These averaging procedures represent best practice, but in this present paper we have used an existing hydrographic atlas which has not been averaged in a thickness-weighted manner. While this is undesirable, this difference is unlikely to impact our results, given all the other limitations in the data.

Replacing the thickness-weighted mean horizontal velocity for the Eulerian-mean horizontal velocity and the parameterization of the quasi-Stokes velocity of Equation (A11), and adding this to Equation (A9) results in the final expression for the cross-contour velocity, as it is used in this paper:

$$
\begin{aligned}
v^{\perp} = {} & \frac{1}{|\nabla_n \hat{\Theta}|} \gamma_z \nabla_n \cdot \left(\gamma_z^{-1} K \nabla_n \hat{\Theta} \right) + \frac{1}{|\nabla_n \hat{\Theta}|} K g N^{-2} \hat{\Theta}_z \left(C_b^{\Theta} \nabla_n \hat{\Theta} \cdot \nabla_n \hat{\Theta} + T_b^{\Theta} \nabla_n \hat{\Theta} \cdot \nabla_n P \right) \\
& + \frac{1}{|\nabla_n \hat{\Theta}|} D \beta \hat{\Theta} g N^{-2} \left(\hat{\Theta}_z \hat{S}_{Azz} - \hat{S}_{Az} \hat{\Theta}_{zz} \right) - \left(\frac{K_{GM} \nabla_z \overline{\gamma}}{\overline{\gamma}_z} \right)_z \cdot \frac{\nabla_n \hat{\Theta}}{|\nabla_n \hat{\Theta}|}
\end{aligned}
\qquad \text{(A12)}
$$

This equation has previously also been used, in slightly different form, by other studies (E.g. McDougall (1984); IOC et al. (2010); Zika et al. (2010a)).

Window size for vertical derivatives	Window size for final terms	**Estimated** D (All values $\times 10^{-4}$)			**Estimated** K		
		25^{th} percentile	Median	75^{th} percentile	25^{th} percentile	Median	75^{th} percentile
1	7	2,00	3,02	3,42	581	642	667
1	11	4,38	5,80	6,08	1000	1080	1103
1	15	2,51	3,00	3,17	1305	1365	1391
3	7	0,32	0,68	1,31	495	514	545
3	11	2,46	3,32	3,69	1062	1152	1194
3	15	1,40	1,61	1,73	1304	1346	1368
5	7	1,52	2,06	2,39	601	647	672
5	11	2,35	2,91	3,13	1165	1232	1262
5	15	1,70	1,93	2,03	1257	1289	1305

TABLE B1. Estimates obtained with various window sizes in the smoothing process for calculated vertical derivatives and the final terms of the Watermass Transformation equation. All estimated values are in $[m^2/s]$.

APPENDIX B

Sensitivity studies

B1. Sensitivity of estimates to data smoothing

In Section 3 it was highlighted that some smoothing was applied when calculating vertical derivatives of Θ, S_A and γ_n, as well as to the final terms that form the Watermass Transformation equation. In this section, the sensitivity of the final estimates to this degree of smoothing is explored. Table B1 shows for a random location in the study area (27° N, 330° E), the estimates with various amounts of smoothing. The window size of the running mean smoothing process is varied for both smoothing processes. The window size is the indication how many points are taken into account for the calculation of the mean value. The estimates are obtained following the steps as in Section 4.

Besides the values in Table B1, we also made a visual inspection of the smoothed profiles and of the proportion of negative diffusivities (that passed the χ-criteria of Eq. 17) obtained in our inversions. We found that for the least amount of smoothing the diffusivity estimates were lower and there were more negative values. Therefore we deduced that some amount of smoothing was desirable. Of the three choices we made of window size, we found that the large and intermediate window gave similar results, and so we selected the window sizes of 3 and 11 points.

B2. Sensitivity of the τ-criterium

The combinations of depths z_u and z_l, that are used in the inversion process of the SIM fullfill the condition $\tau_u - \tau_l \approx 0$. In the process of selecting the pairs, it is approximated that this is the case for combinations of depths for which $\tau_u - \tau_l < crt$. The results presented in Sections 4, 5 and 6 the crt was set to 0.0075 $[rad]$. In this Appendix, the sensitivity of the results with respect to this choice is analysed.

The number of pairs, the reduction based on the signal-to-noise criteria, and the results for a range of different crt values will be compared. The crt values for 0.004, 0.0075, 0.015 and 0.05 are selected for this.

a. Number of pairs

When increasing the critical value for $\tau_u - \tau_l \approx 0$, the number of pairs increases (Fig. B1). Also the number of pairs that remain after the signal-to-noise criteria increases (Fig. B2). However, they differ less from each other than without also using this criteria. For the smallest crt-value the number of available pairs, after the signal-to-noise removal, starts to become too low for some locations to get an estimate. We consider this too strict. In general, more pairs correspond to more equations that can be used in the inversion process. However, it can be expected that the error that these equations contain also increases with a larger crt-value, as the approximation of $\tau_u - \tau_l \approx 0$ becomes less accurate for larger crt values.

b. Accuracy of the estimates

A scatterplot of the estimated values compared to the maximum from the structure function, show that the estimated values for K and D are not too sensitive for the choice of crt (Figs. B3 and B4). In some cases the values for K^{inv} are small compared to the maximum from the structure function (B3d). A possible explanation is that with larger critical values, more error is introduced by the dataset allowing for a wider range of estimates.

Overall the SIM is not very sensitive to the choice of crt. Using a too small value can reduce the number of equations we can construct (fewer pairs). A too large critical value introduces more error and a larger spread of the results. The chosen value $crt = 0.0075$, as used in Sections 4,5 and 6 is therefore a reasonable choice.

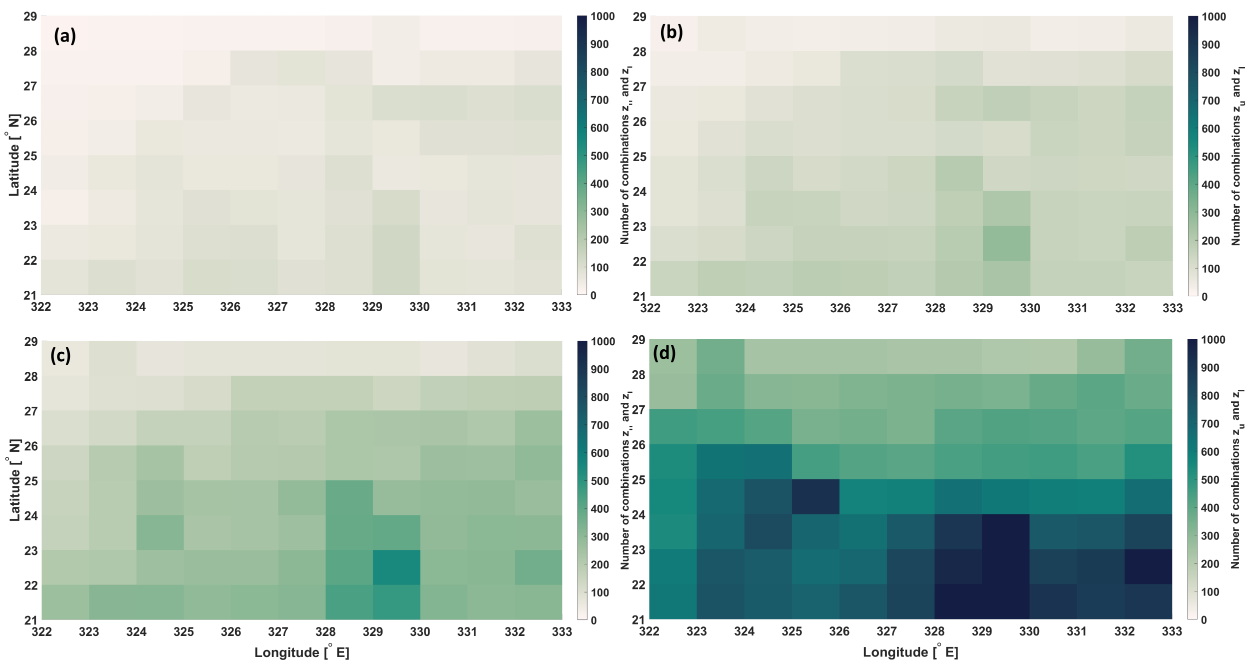

595 FIG. B1. The number of pairs based on the *crt* criterium. a) *crt* = 0.004, b) *crt* = 0.0075, c) *crt* = 0.015, d)
596 *crt* = 0.05. The maximum number of pairs in panel d) is 1283

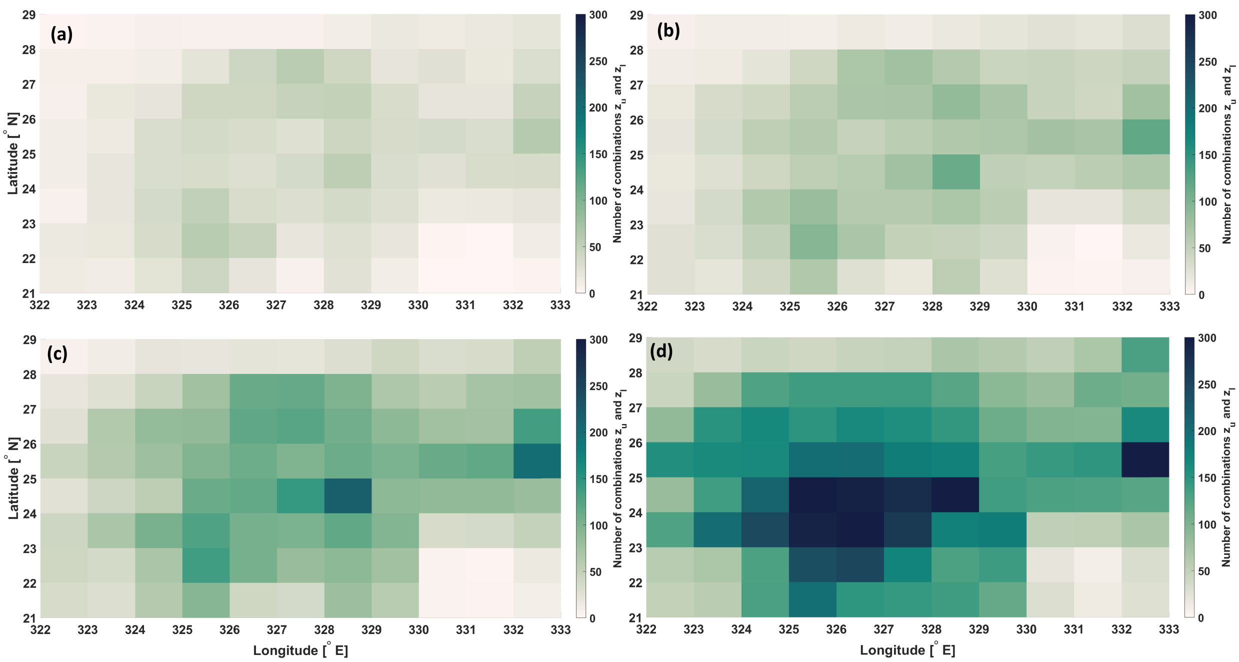

FIG. B2. The number of pairs based on the *crt* criterium, after reduction based on the signal-to-noise criteria as described in Section 4. a) $crt = 0.004$, b) $crt = 0.0075$, c) $crt = 0.015$, d) $crt = 0.05$. The maximum number of pairs in panel d) is 416.

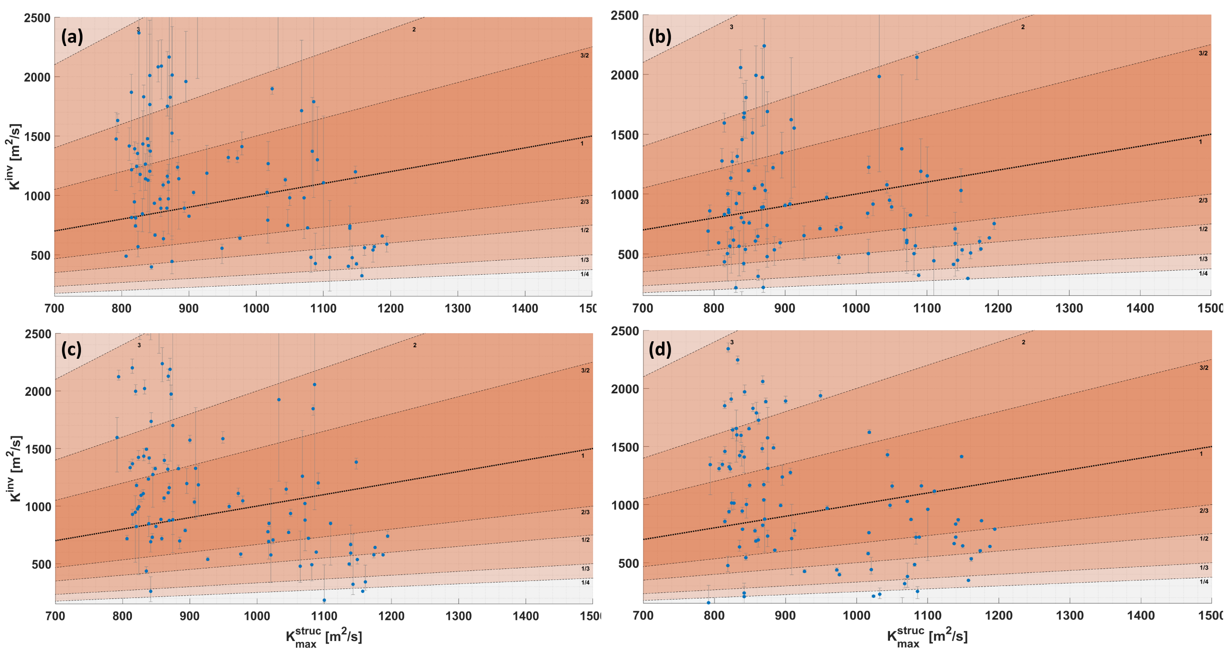

FIG. B3. The values for K^{inv} plotted against the value of the used structure function. With a) $crt = 0.004$, b) $crt = 0.0075$, c) $crt = 0.015$, d) $crt = 0.05$. The orange shading represents the ratio between estimated value and the value of the structure function. Gray lines mark the uncertainty of the estimate, given by the 25^{th} and 75^{th} percentiles.

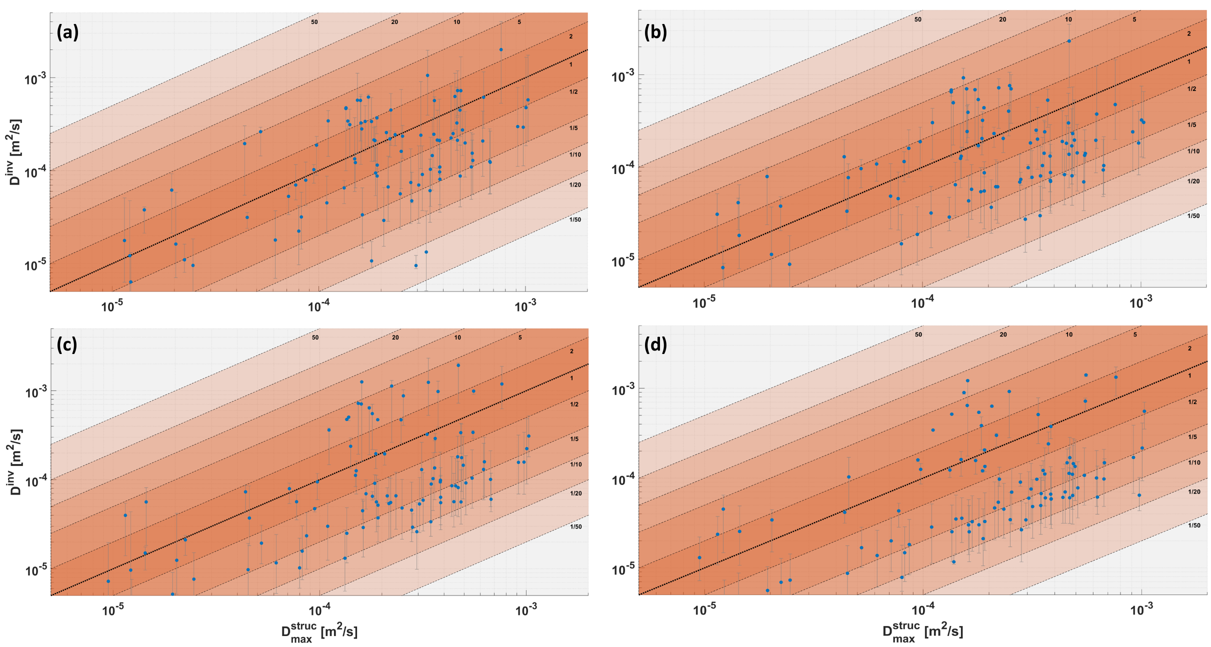

FIG. B4. The values for D^{inv} plotted against the value of the used structure function. With a) $crt = 0.004$, b) $crt = 0.0075$, c) $crt = 0.015$, d) $crt = 0.05$. The orange shading represents the ratio between estimated value and the value of the structure function. Gray lines mark the uncertainty of the estimate, given by the 25^{th} and 75^{th} percentiles.

APPENDIX C

Range of solutions

Section 4e explored a wide range of input variables to the inversion, which was aimed at gaining a physically realistic estimate for K and D. Despite the removal of equations that contained too much noise, based on the signal to noise criteria of Section 4c, the estimates by this sensitivity analysis spanned a wide range. This solution space contained also negative estimates. While mathematically, these estimates are valid, these are considered to be outside the space that is physically realistic. This is because the results are obtained from an annual mean gridded climatology that inherently represents an ocean mean state in which diffusion is down gradient. For this reason an additional positivity constraint was added besides the chi-criteria (see Sec. 4e). Without this constraint, about 45% of the estimates for D^{inv} are negative, while the estimates for K^{inv} are practically unaffected. Fig. C1 shows the results without the constraint. The estimates with this positivity constraint were shown in Fig. 6.

The casts that return negative estimates also show a larger spread of the estimates from the sensitivity analysis. This can indicate that these casts possibly are still more affected by noise in the data or that it would be beneficial if more equations were available for the inversion. Either way, these estimates should be treated with caution.

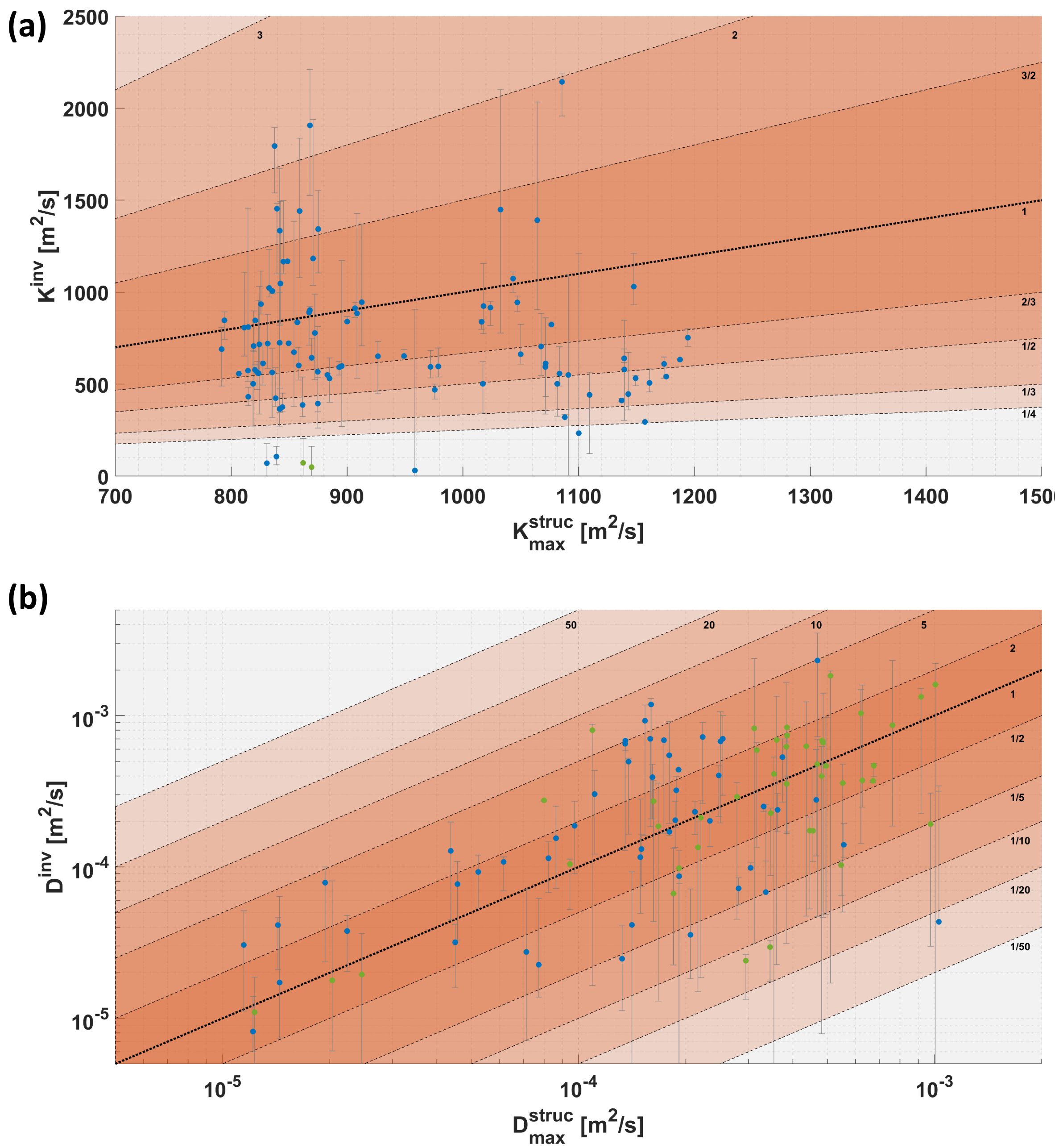

FIG. C1. Results without the positivity constraint. With (a) K^{inv} without constraint. (b) D^{inv} without constraint, negative estimates are shown as absolute values, marked with a green dot. For both panels, whiskers mark the 25^{th} and 75^{th} percentiles.

APPENDIX D

Other structure functions

Here we test the sensitivity of the SIM to the choice of structure function used by estimating K and D using different structure functions according to the following set-up:

- **Original**: The structure functions are as presented in Sections 3 and the results of Fig. 7.
- **Test 1**: For K the structure is based on Cole et al. (2015). But as their data reaches to 1700 m depth, we have linearly extrapolated this to be 0 at the ocean floor. This is combined with the structure function of De Lavergne et al. (2020) for D.
- **Test 2**: For K the used structure function is the same as presented in Section 3 and the results of Fig. 7, so the study by Groeskamp et al. (2020). This is combined with a profile for D based on a linear interpolation from 10^{-5} $[m^2/s]$ at the surface to 5×10^{-5} $[m^2/s]$ at the bottom.
- **Test 3**: A constant value of 1000 $[m^2/s]$ is used for K and a constant value of 5×10^{-5} $[m^2/s]$ is used for D as structure functions.

The choice of structure function influences the results of both K and D and affects the final estimates by impacting the signal to noise criteria and a-priori estimates such as $\mathbf{x_0}$. However, these tests clearly indicate that the SIM finds solutions that are not restricted to the original magnitude of the structure functions, even while the shape is maintained by construction (Fig. D1).

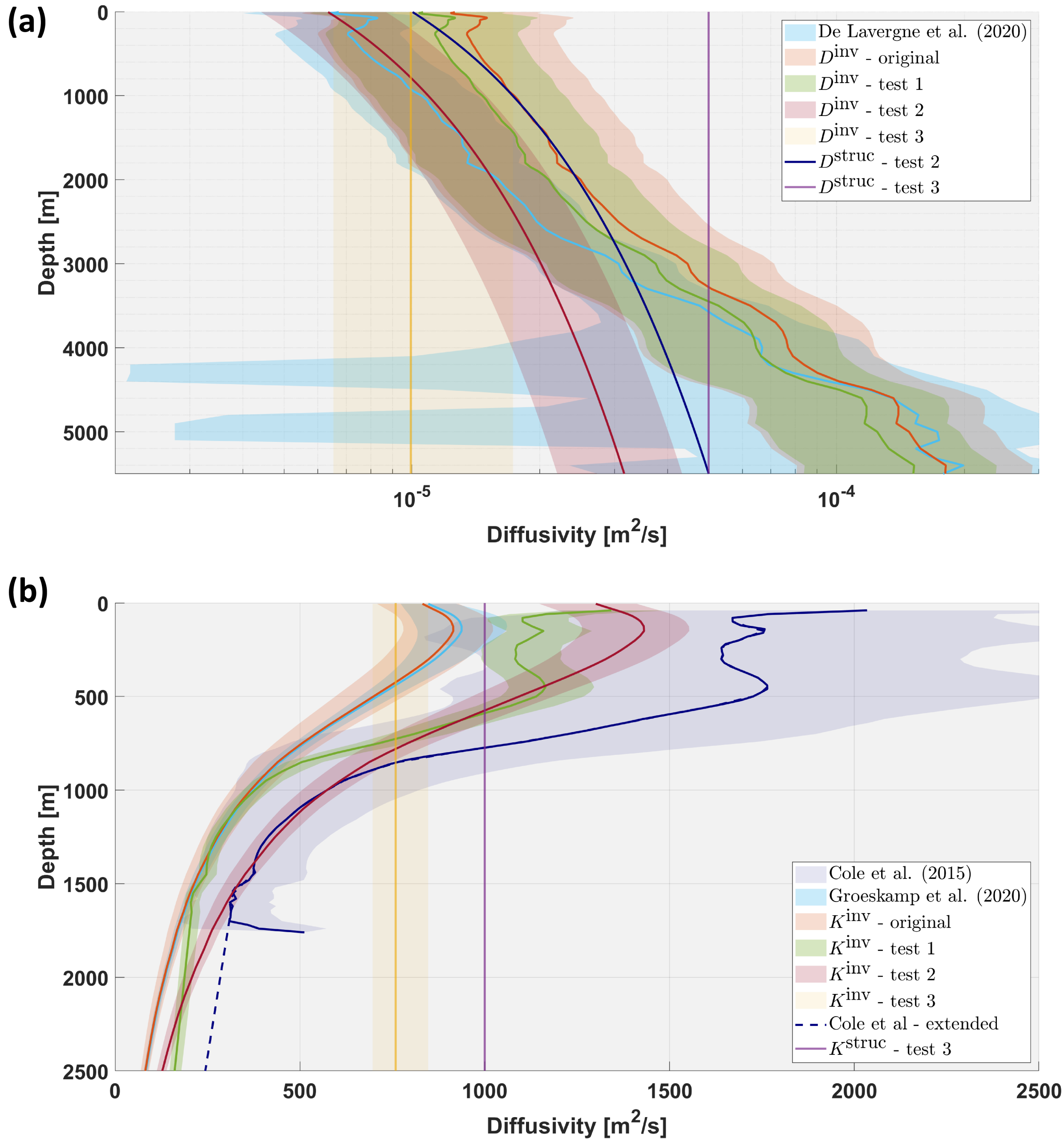

FIG. D1. Estimtes of K and D from the SIM, using different structure functions, including those presented in Section 6. The estimates of the SIM are given by their median values, the shadings indicate the 25^{th} and 75^{th} percentiles. For the studies of Cole et al. (2015) and De Lavergne et al. (2020) and Groeskamp et al. (2020), the shading indicates the uncertainty given by the study. In (a), the results of D^{inv} are presented, similarly in (b) the results of K^{inv}.

References

Abernathey, R., A. Gnanadesikan, M. A. Pradal, and M. A. Sundermeyer, 2021: Isopycnal mixing. *Ocean Mixing: Drivers, Mechanisms and Impacts*, Elsevier, 215–256, https://doi.org/10.1016/B978-0-12-821512-8.00016-5.

Abernathey, R. P., and J. Marshall, 2013: Global surface eddy diffusivities derived from satellite altimetry. *Journal of Geophysical Research: Oceans*, **118**, 901–916, https://doi.org/10.1002/jgrc.20066.

Alford, M. H., J. A. Mackinnon, H. L. Simmons, and J. D. Nash, 2016: Near-inertial internal gravity waves in the ocean. *Annual Review of Marine Science*, **8**, 95–123, https://doi.org/10.1146/annurev-marine-010814-015746.

Armi, L., and H. Stommel, 1983: Four views of a portion of the north atlantic subtropical gyre. *Journal of Physical Oceanography*, **13**, 828–857, https://doi.org/10.1175/1520-0485(1983)013⟨0828:FVOAPO⟩2.0.CO;2.

Barker, P. M., and T. J. McDougall, 2017: Stabilizing hydrographic profiles with minimal change to the water masses. *Journal of Atmospheric and Oceanic Technology*, **34**, 1935–1945, https://doi.org/10.1175/JTECH-D-16-0111.1.

Clément, L., E. L. McDonagh, J. M. Gregory, Q. Wu, A. Marzocchi, J. D. Zika, and A. J. Nurser, 2022: Mechanisms of ocean heat uptake along and across isopycnals. *Journal of Climate*, **35**, 4885–4904, https://doi.org/10.1175/JCLI-D-21-0793.1.

Cole, S. T., C. Wortham, E. Kunze, and W. B. Owens, 2015: Eddy stirring and horizontal diffusivity from argo float observations: Geographic and depth variability. *Geophysical Research Letters*, **42**, 3989–3997, https://doi.org/10.1002/2015GL063827.

De Lavergne, C., S. Falahat, G. Madec, F. Roquet, J. Nycander, and C. Vic, 2019: Toward global maps of internal tide energy sinks. *Ocean Modelling*, **137**, 52–75, https://doi.org/10.1016/j.ocemod.2019.03.010.

De Lavergne, C., S. Groeskamp, J. Zika, and H. L. Johnson, 2022: The role of mixing in the large-scale ocean circulation. *Ocean Mixing: Drivers, Mechanisms and Impacts*, M. Meredith, and A. Naveira Garabato, Eds., Elsevier, 35–63, https://doi.org/10.1016/B978-0-12-821512-8.00010-4.

De Lavergne, C., and Coauthors, 2020: A parameterization of local and remote tidal mixing. *Journal of Advances in Modeling Earth Systems*, **12**, https://doi.org/10.1029/2020MS002065.

Ferrari, R., and M. Nikurashin, 2010: Suppression of eddy diffusivity across jets in the southern ocean. *Journal of Physical Oceanography*, **40**, 1501–1519, https://doi.org/10.1175/2010JPO4278.1.

Fox-Kemper, B., and Coauthors, 2019: Challenges and prospects in ocean circulation models. *Frontiers in Marine Science*, **6**, https://doi.org/10.3389/fmars.2019.00065.

Ganachaud, A., and C. Wunsch, 2000: Improved estimates of global ocean circulation, heat transport and mixing from hydrographic data. *Nature*, **408**, 453–457, https://doi.org/10.1038/35044048.

Gent, P. R., J. Willebrand, T. J. McDougall, and J. C. McWilliams, 1995: Parameterizing eddy-induced tracer transports in ocean circulation models. *Journal of Physical Oceanography*, **25**, 463–474, https://doi.org/10.1175/1520-0485(1995)025⟨0463:PEITTI⟩2.0.CO;2.

Graham, F. S., and T. J. McDougall, 2013: Quantifying the nonconservative production of conservative temperature, potential temperature, and entropy. *Journal of Physical Oceanography*, **43**, 838–862, https://doi.org/10.1175/JPO-D-11-0188.1.

Gray, A. R., and S. C. Riser, 2014: A global analysis of sverdrup balance using absolute geostrophic velocities from argo. *Journal of Physical Oceanography*, **44**, 1213–1229, https://doi.org/10.1175/JPO-D-12-0206.1.

Griffies, S. M., 1998: The gent-mcwilliams skew flux. *Journal of Physical Oceanography*, **28**, 831–841, https://doi.org/10.1175/1520-0485(1998)028⟨0831:TGMSF⟩2.0.CO;2.

Groeskamp, S., R. P. Abernathey, and A. Klocker, 2016: Water mass transformation by cabbeling and thermobaricity. *Geophysical Research Letters*, **43**, https://doi.org/10.1002/2016GL070860.

Groeskamp, S., P. M. Barker, T. J. McDougall, R. P. Abernathey, and S. M. Griffies, 2019: Venm: An algorithm to accurately calculate neutral slopes and gradients. *Journal of Advances in Modeling Earth Systems*, **11**, 1917–1939, https://doi.org/10.1029/2019MS001613.

Groeskamp, S., and D. Iudicone, 2018: The effect of air-sea flux products, shortwave radiation depth penetration, and albedo on the upper ocean overturning circulation. *Geophysical Research Letters*, **45**, 9087–9097, https://doi.org/10.1029/2018GL078442.

Groeskamp, S., J. H. LaCasce, T. J. McDougall, and M. Rogé, 2020: Full-depth global estimates of ocean mesoscale eddy mixing from observations and theory. *Geophysical Research Letters*, **47**, 1–12, https://doi.org/10.1029/2020GL089425.

Groeskamp, S., B. M. Sloyan, J. D. Zika, and T. J. McDougall, 2017: Mixing inferred from an ocean climatology and surface fluxes. *Journal of Physical Oceanography*, **47**, 667–687, https://doi.org/10.1175/JPO-D-16-0125.1.

Groeskamp, S., J. D. Zika, B. M. Sloyan, T. J. Mcdougall, and P. C. Mcintosh, 2014: A thermohaline inverse method for estimating diathermohaline circulation and mixing. *Journal of Physical Oceanography*, **44**, 2681–2697, https://doi.org/10.1175/JPO-D-14-0039.1.

Hautala, S. L., 2018: The abyssal and deep circulation of the northeast pacific basin. *Progress in Oceanography*, **160**, 68–82, https://doi.org/10.1016/j.pocean.2017.11.011.

Holmes, R. M., S. Groeskamp, K. D. Stewart, and T. J. McDougall, 2022: Sensitivity of a coarse-resolution global ocean model to a spatially variable neutral diffusivity. *Journal of Advances in Modeling Earth Systems*, **14**, https://doi.org/10.1029/2021MS002914.

IOC, SCOR, and IAPSO, 2010: The international thermodynamic equation of seawater – 2010: Calculation and use of thermodynamic properties. *Manuals and Guides No. 56*, Intergovernmental Oceanographic Commission, 196.

Jackett, D. R., and T. J. McDougall, 1997: A neutral density variable for the world's oceans. *Journal of Physical Oceanography*, **27**, 237–263, https://doi.org/10.1175/1520-0485(1997)027⟨0237:ANDVFT⟩2.0.CO;2.

Jenkins, W. J., 1987: 3h and 3he in the beta triangle: Observations of gyre ventilation and oxygen utilization rates. *Journal of Physical Oceanography*, **17**, 763–783, https://doi.org/10.1175/1520-0485(1987)017⟨0763:AITBTO⟩2.0.CO;2.

Jenkins, W. J., 1998: Studying subtropical thermocline ventilation and circulation using tritium and 3 he. *Journal of Geophysical Research: Oceans*, **103**, 15 817–15 831, https://doi.org/10.1029/98jc00141.

Joyce, T. M., J. R. Luyten, A. Kubryakov, F. B. Bahr, and J. S. Pallant, 1998: Meso-to large-scale structure of subducting water in the subtropical gyre of the eastern north atlantic ocean. *Journal of Physical Oceanography*, **28**, 40–61, https://doi.org/10.1175/1520-0485(1998)028⟨0040:MTLSSO⟩2.0.CO;2.

Killworth, P. D., 1986: A bernoulli inverse method for determining the ocean circulation. *Journal of Physical Oceanography*, **16**, 2031–2051, https://doi.org/10.1175/1520-0485(1986)016⟨2031:ABIMFD⟩2.0.CO;2.

Klocker, A., and R. Abernathey, 2014: Global patterns of mesoscale eddy properties and diffusivities. *Journal of Physical Oceanography*, **44**, 1030–1046, https://doi.org/10.1175/JPO-D-13-0159.1.

Klocker, A., and T. J. McDougall, 2010: Influence of the nonlinear equation of state on global estimates of dianeutral advection and diffusion. *Journal of Physical Oceanography*, **40**, 1690–1709, https://doi.org/10.1175/2010JPO4303.1.

LaCasce, J. H., and S. Groeskamp, 2020: Baroclinic modes over rough bathymetry and the surface deformation radius. *Journal of Physical Oceanography*, **50**, 2835–2847, https://doi.org/10.1175/JPO-D-20-0055.1.

Lebedev, K. V., H. Yoshinari, N. A. Maximenko, and P. W. Hacker, 2007: Yomaha'07: Velocity data assessed from trajectories of argo floats at parking level and at the sea surface.

Ledwell, J. R., A. J. Watson, and C. S. Law, 1993: Evidence for slow mixing across the pycnocline from an open-ocean tracer-release experiment. *Nature*, **364**, 701–703, https://doi.org/10.1038/364701a0.

Ledwell, J. R., A. J. Watson, and C. S. Law, 1998: Mixing of a tracer in the pycnocline. *Journal of Geophysical Research*, **103**, 21 499–21 529, https://doi.org/10.1029/98JC01738.

Legg, S., 2021: Mixing by oceanic lee waves. *Annual Review of Fluid Mechanics*, **53**, 173–201, https://doi.org/10.1146/annurev-fluid-051220-043904.

Locarnini, R., and Coauthors, 2019: World ocean atlas 2018, volume 1: Temperature. *NOAA Atlas NESDIS 81*, A. Mishonov Technical Editor, 52.

MacGilchrist, G. A., H. L. Johnson, D. P. Marshall, C. Lique, M. Thomas, L. C. Jackson, and R. A. Wood, 2020: Locations and mechanisms of ocean ventilation in the high-latitude north atlantic in an eddy-permitting ocean model. *Journal of Climate*, **33**, 10 113–10 131, https://doi.org/10.1175/JCLI-D-20-0191.1.

Mackay, N., C. Wilson, J. Zika, and N. P. Holliday, 2018: A regional thermohaline inverse method for estimating circulation and mixing in the arctic and subpolar north atlantic. *Journal of Atmospheric and Oceanic Technology*, **35**, 2383–2403, https://doi.org/10.1175/JTECH-D-17-0198.1.

MacKinnon, J., 2013: Mountain waves in the deep ocean. *Nature*, **501**, 321–322, https://doi.org/10.1038/501321a.

McDougall, T. J., 1984: The relative roles of diapycnal and isopycnal mixing on subsurface water mass conversion. *Journal of Physical Oceanography*, **14**, 1577–1589, https://doi.org/10.1175/1520-0485(1984)014⟨1577:TRRODA⟩2.0.CO;2.

McDougall, T. J., 1987a: Neutral surfaces. *Journal of Physical Oceanography*, **17**, 1950–1964, https://doi.org/10.1175/1520-0485(1987)017⟨1950:NS⟩2.0.CO;2.

McDougall, T. J., 1987b: Thermobaricity, cabbeling, and water-mass conversion. *Journal of Geophysical Research*, **92**, 5448–5464, https://doi.org/10.1029/JC092iC05p05448.

McDougall, T. J., 1991: Water mass analysis with three conservative variables. *Journal of Geophysical Research: Oceans*, **96**, 8687–8693, https://doi.org/10.1029/90JC02739.

McDougall, T. J., 1995: The influence of ocean mixing on the absolute velocity vector. *Journal of Physical Oceanography*, **25**, 705–725, https://doi.org/10.1175/1520-0485(1995)025⟨0705:TIOOMO⟩2.0.CO;2.

McDougall, T. J., 2003: Potential enthalpy: A conservative oceanic variable for evaluating heat content and heat fluxes. *Journal of Physical Oceanography*, **33**, 945–963, https://doi.org/10.1175/1520-0485(2003)033⟨0945:PEACOV⟩2.0.CO;2.

McDougall, T. J., and P. M. Barker, 2011: Getting started with teos-10 and the gibbs seawater (gsw) oceanographic toolbox. SCOR/IAPSO WG127, 28 pp.

McDougall, T. J., S. Groeskamp, and S. M. Griffies, 2014: On geometrical aspects of interior ocean mixing. *Journal of Physical Oceanography*, **44**, 2164–2175, https://doi.org/10.1175/JPO-D-13-0270.1.

McDougall, T. J., D. R. Jackett, F. J. Millero, R. Pawlowicz, and P. M. Barker, 2012: A global algorithm for estimating absolute salinity. *Ocean Science*, **8**, 1123–1134, https://doi.org/10.5194/os-8-1123-2012.

McDougall, T. J., and P. C. McIntosh, 2001: The temporal-residual-mean velocity. part ii: Isopycnal interpretation and the tracer and momentum equations. *Journal of Physical Oceanography*, **31**, 1222–1246, https://doi.org/10.1175/1520-0485(2001)031⟨1222:TTRMVP⟩2.0.CO;2.

McIntosh, P. C., and S. R. Rintoul, 1997: Do box inverse models work? *Journal of Physical Oceanography*, **27**, 291–308, https://doi.org/10.1175/1520-0485(1997)027⟨0291:DBIMW⟩2.0.CO;2.

Melet, A. V., R. Hallberg, and D. P. Marshall, 2022: The role of ocean mixing in the climate system. *Ocean Mixing: Drivers, Mechanisms and Impacts*, Elsevier, 5–34, https://doi.org/10.1016/B978-0-12-821512-8.00009-8.

Menke, W., 2018: *Geophysical Data Analysis: Discrete Inverse Theory*. 3rd ed., Elsevier Science & Technology, 293 pp., https://ebookcentral.proquest.com/lib/uunl/detail.action?docID=5347046.

Millero, F. J., R. Feistel, D. G. Wright, and T. J. McDougall, 2008: The composition of standard seawater and the definition of the reference-composition salinity scale. *Deep-Sea Research Part I*, **55**, 50–72, https://doi.org/10.1016/j.dsr.2007.10.001.

Moum, J. N., 2021: Variations in ocean mixing from seconds to years. *Annual Review of Marine Science*, **13**, 201–226, https://doi.org/10.1146/annurev-marine-031920-122846.

Munk, W., and C. Wunsch, 1998: Abyssal recipes ii: energetics of tidal and wind mixing. *Deep-Sea Research I*, **45**, 1977–2010, https://doi.org/10.1016/S0967-0637(98)00070-3.

Nurser, A. J. G., and S. M. Griffies, 2019: Relating the diffusive salt flux just below the ocean surface to boundary freshwater and salt fluxes. *Journal of Physical Oceanography*, **49**, 2365–2376, https://doi.org/10.1175/JPO-D-19-0037.1.

Oakey, N., 1982: Determination of the rate of dissipation of turbulent energy from simultaneous temperature and velocity shear microstructure measurements. *Journal of Physical Oceanography*, **12**, 256–271, https://doi.org/10.1175/1520-0485(1982)012%3C0256:DOTROD%3E2.0.CO;2.

Pawlowicz, R., T. McDougall, R. Feistel, and R. Tailleux, 2012: An historical perspective on the development of the thermodynamic equation of seawater-2010. *Ocean Science*, **8**, 161–174, https://doi.org/10.5194/os-8-161-2012.

Pradal, M.-A., and A. Gnanadesikan, 2014: How does the redi parameter for mesoscale mixing impact global climate in an earth system model? *Journal of Advances in Modeling Earth Systems*, **6**, 586–601, https://doi.org/10.1002/2013MS000273.

Prandtl, L., 1925: Report on investigation of developed turbulence. *Journal of Applied Mathematics and Mechanics*, **5**, 136–139.

Redi, M. H., 1982: Oceanic isopycnal mixing by coordinate rotation. *Journal of Physical Oceanography*, **12**, 1154–1158, https://doi.org/10.1175/1520-0485(1982)012⟨1154:OIMBCR⟩2.0.CO;2.

Roach, C. J., D. Balwada, and K. Speer, 2018: Global observations of horizontal mixing from argo float and surface drifter trajectories. *Journal of Geophysical Research: Oceans*, **123**, 4560–4575, https://doi.org/10.1029/2018JC013750.

Schott, F., and H. Stommel, 1978: Beta spirals and absolute velocities in different oceans. *Deep-Sea Research*, **25**, 961–1010, https://doi.org/10.1016/0146-6291(78)90583-0.

Sloyan, B. M., and S. R. Rintoul, 2000: Estimates of area-averaged diapycnal fluxes from basin-scale budgets. *Journal of Physical Oceanography*, **30**, 2320–2341, https://doi.org/10.1175/1520-0485(2000)030⟨2320:EOAADF⟩2.0.CO;2.

Sloyan, B. M., and S. R. Rintoul, 2001: The southern ocean limb of the global deep overturning circulation. *Journal of Physical Oceanography*, **31**, 143–173, https://doi.org/10.1175/1520-0485(2001)031⟨0143:TSOLOT⟩2.0.CO;2.

Smith, K. S., and J. Marshall, 2009: Evidence for enhanced eddy mixing at middepth in the southern ocean. *Journal of Physical Oceanography*, **39**, 50–69, https://doi.org/10.1175/2008JPO3880.1.

Spall, M. A., P. L. Richardson, and J. Price, 1993: Advection and eddy mixing in the mediterranean salt tongue. *Journal of Marine Research*, **51**, 797–818.

Stommel, H., and F. Schott, 1977: The beta spiral and the determination of the absolute velocity field from hydrographic station data. *Deep-Sea Research*, **24**, 325–329, https://doi.org/10.1016/0146-6291(77)93000-4.

Tatebe, H., Y. Tanaka, Y. Komuro, and H. Hasumi, 2018: Impact of deep ocean mixing on the climatic mean state in the southern ocean. *Scientific Reports*, **8**, https://doi.org/10.1038/s41598-018-32768-6.

Toole, J. M., K. L. Polzin, and R. W. Schmitt, 1994: Estimates of diapycnal mixing in the abyssal ocean. *Science*, **264**, 1120–1123, https://doi.org/10.1126/science.264.5162.1120.

Waterhouse, A. F., and Coauthors, 2014: Global patterns of diapycnal mixing from measurements of the turbulent dissipation rate. *Journal of Physical Oceanography*, **44**, 1854–1872, https://doi.org/10.1175/JPO-D-13-0104.1.

Whalen, C. B., J. A. MacKinnon, and L. D. Talley, 2018: Large-scale impacts of the mesoscale environment on mixing from wind-driven internal waves. *Nature Geoscience*, **11**, 842–847, https://doi.org/10.1038/s41561-018-0213-6.

Wright, D. G., R. Pawlowicz, T. J. McDougall, R. Feistel, and G. M. Marion, 2011: Absolute salinity, ”density salinity” and the reference-composition salinity scale: Present and future use in the seawater standard teos-10. *Ocean Science*, **7**, 1–26, https://doi.org/10.5194/os-7-1-2011.

Wunsch, C., 1978: The north atlantic general circulation west of 50 w determined by inverse methods. *Reviews of Geophysics and Space Physics*, **16**, 583–620, https://doi.org/10.1029/RG016i004p00583.

Zhang, H.-M., and N. G. Hogg, 1992: Circulation and water mass balance in the brazil basin. *Journal of Marine Research*, **50**, 385–420, https://doi.org/10.1357/002224092784797629.

Zika, J. D., and T. J. McDougall, 2008: Vertical and lateral mixing processes deduced from the mediterranean water signature in the north atlantic. *Journal of Physical Oceanography*, **38**, 164–176, https://doi.org/10.1175/2007JPO3507.1.

Zika, J. D., T. J. McDougall, and B. M. Sloyan, 2010a: A tracer-contour inverse method for estimating ocean circulation and mixing. *Journal of Physical Oceanography*, **40**, 26–47, https://doi.org/10.1175/2009JPO4208.1.

Zika, J. D., T. J. McDougall, and B. M. Sloyan, 2010b: Weak mixing in the eastern north atlantic: An application of the tracer-contour inverse method. *Journal of Physical Oceanography*, **40**, 1881–1893, https://doi.org/10.1175/2010JPO4360.1.

Zika, J. D., B. M. Sloyan, and T. J. McDougall, 2009: Diagnosing the southern ocean overturning from tracer fields. *Journal of Physical Oceanography*, **39**, 2926–2940, https://doi.org/10.1175/2009JPO4052.1.

Zweng, M., J. Reagan, D. Seidov, T. Boyer, R. Locarcini, H. Garcia, and A. Mishonov, 2019: World ocean atlas 2018, volume 2: Salinity. *NOAA Atlas NESDIS 82*, A. Mishonov Technical Editor, 50.